University of Nevada, Reno

Vegetation Canopy Cover Effects on Sediment and Salinity Loading in the Upper Colorado River Basin Mancos Shale Formation, Price, Utah

A thesis submitted in partial fulfillment of the requirements
for the degree of Master of Science in Hydrogeology

by

Erik M. Cadaret

Dr. Kenneth C. McGwire/Thesis Advisor

December, 2015

THE GRADUATE SCHOOL

We recommend that the thesis
prepared under our supervision by

ERIK M. CADARET

Entitled

Vegetation Canopy Cover Effects on Sediment and Salinity Loading in the Upper Colorado River Basin Mancos Shale Formation, Price, Utah

be accepted in partial fulfillment of the
requirements for the degree of

MASTER OF SCIENCE

Kenneth C. McGwire, Ph.D., Advisor

Robert R. Blank, Ph.D., Committee Member

Mark A. Weltz, Ph.D., Committee Member

Laurel Saito, Ph.D., Graduate School Representative

David W. Zeh, Ph. D., Dean, Graduate School

December, 2015

Abstract

With future climate change and increased water demand and scarcity in the Colorado River Basin, the Bureau of Reclamation estimates that the costs of salinity damage will increase for Colorado River users and will exacerbate the current salinity challenges. This study focuses on saline and sodic soils associated with the Mancos Shale formation in order to investigate the mechanisms driving sediment and salinity loads in the Price-San Rafael River Basin of the upper Colorado River. A Walnut Gulch rainfall simulator was operated with a variety of slope angles and rainfall intensities at two field sites (Price, Dry-X) near Price, Utah in order to evaluate how the amount and spatial distribution of vegetation affects salinity in runoff. For each simulated rainfall event, the time-varying concentrations of major cations, anions, and sediment in runoff were measured.

Principal component analysis revealed that the two field sites are generally different in runoff water chemistry and soil chemistry, likely due to the difference in parent material and soil indicative of their location on different geologic members. The Dry-X site also has substantially greater total dissolved solids (TDS) and sediment in runoff, soil sodium absorption ratio (SAR), and soil cation exchange capacity (CEC) than the Price site.

Despite these differences, a consistent positive linear relationship between the plot-averaged sediment and TDS concentration was found across both sites.

The Rangeland Hydrology Erosion Model (RHEM) was calibrated to provide unbiased estimates of sediment in runoff from 23 runs of the rainfall simulator. RHEM simulated the plot-plot variability best at Dry-X compared to Price. Sensitivity analysis of the RHEM input parameters showed that the splash and sheet erodibility coefficient (Kss) and the effective saturated conductivity coefficient (Ke) had the largest influence on the model's sediment and discharge outputs, respectively. The regression that predicted TDS concentration from sediment was applied to RHEM outputs to show that the model could be used to provide salinity estimates for different storm intensities on this part of the Mancos Shale.

The potential influence of vegetation canopy cover on sediment production from these two sites was inferred by running RHEM with canopy cover values ranging from 0% to 100%. This changed sediment output by 111% to -91% relative to the present vegetation cover. Measures of the geometry of soil and vegetation patches at Dry-X, such as fractal dimension index and proximity index, showed a relationship to error residuals from RHEM. As the vegetation becomes less isolated, more uniform, and the tortuosity of the bare soil area increases, observed sediment decreases relative to RHEM predictions.

The results of this study will help land management agencies assess the feasibility of mitigation strategies for reducing sediment and salinity loads from the saline and sodic soils of the Mancos Shale formation and indicate a possible benefit to incorporating the parameters that describe the spatial pattern of vegetation in RHEM.

Acknowledgements

This thesis project is funded by the Bureau of Land Management (BLM), Bureau of Reclamation (BoR), Desert Research Institute – Division of Earth and Ecosystem Science (DRI-DEES), and United Started Department of Agriculture – Agriculture Research Service (USDA-ARS).

Special thanks to:

- Dr. Ken McGwire for supporting my education and research through DRI-DEES funding. I am thankful for his generosity, guidance, mentorship, and support as committee chair and thesis adviser throughout the duration of this research project and my education
- Committee members Dr. Bob Blank, Dr. Laurel Saito, and Dr. Mark Weltz for their time, energy, and guidance throughout the duration of this research project and my education
- Dr. Mark Weltz and Dr. Cole Rossi for supporting my education and research through BLM and BoR funding
- Dr. Bob Blank and Tye Morgan for their generosity allowing me to work in their soils laboratory and their mentorship on lab procedures

- Alice Boizet for being an excellent lab co-worker and helping me process the runoff water chemistry and soil samples in the soil laboratory during summer of 2014
- Jacob Philips for helping me process runoff water chemistry and soil samples
- Dr. Sayjro K. Nouwakpo for his guidance and collaboration on this research project
- Sandra Li and Todd Adams for their hard work and companionship in the field throughout the duration of this research project
- Dr. Laurel Saito for her hard work and dedication as the Graduate Program of Hydrologic Sciences director to make my experience in the program a great one and for serving on my committee

Table of Contents

List of Tables

List of Figures

1 Introduction

The Colorado River Basin is a primary source of water for seven states in the western U.S. and the Baja region of Mexico (Figure 1). Before substantial settlement of the west occurred, the estimated salt load of the Colorado River was 600 – 700 parts per million (ppm) in the Lower Colorado River Basin [Blackman et al., 1973]. Since the Colorado River Basin Salinity Control Act of 1974 was enacted, salinity has been effectively controlled [Robison et al., 2014], but with climate change and increased water demand and scarcity in the Colorado River Basin, the Bureau of Reclamation estimates that salinity damage costs for Colorado River users will increase and exacerbate the current salinity challenges [Bureau of Reclamation, 2005]. To better understand salinity processes and identify management techniques that may ameliorate salinity problems, studies have been conducted to determine salinity inputs into the river. These studies have shown that up to 55% of the salinity in the Colorado River is from natural sources such as groundwater and surface water [Kenney et al., 2009] in the form of subsurface reemergence [Blackburn and Skau, 1974; Warner et al., 1985; Shirnian-Orlando and Uchrin, 2000].

Figure 1: Geographic map of the Colorado River Basin and areas where water is allocated outside of the basin. Credit: U.S. Bureau of Reclamation.

In Utah, 7 - 15% of the rangeland areas are classified as being in a severely eroding condition; moreover, it is estimated that these areas are responsible for 75 - 90% of the increasing sediment and salt yields [Rasely et al., 1991]. This creates an opportunity to reduce salinity through land and water management activities on rangelands which make up nearly 80% of the land mass in the western United States [Weltz et al., 2008]. The Mancos Shale formation is among these rangeland areas that are in a severely eroding condition. The Mancos Shale spans a wide area in the Upper Colorado River Basin (UCRB) in southeast Utah and has been identified as a major producer of sediment, salinity, and selenium to the Colorado River [Evangelou et al., 1984; Tuttle et al., 2014]. The Price River contributes less than 1% of the water, but approximately 3% of the salt load in the Colorado River, and a substantial part of that salt load comes from the Mancos Shale formation [Rao et al., 1984]. In addition, the majority of the Mancos Shale formation is under the control of the BLM/BoR which provides land managers flexibility to implement plans that may reduce future sediment and salinity loads into the Colorado River (Figure 2).

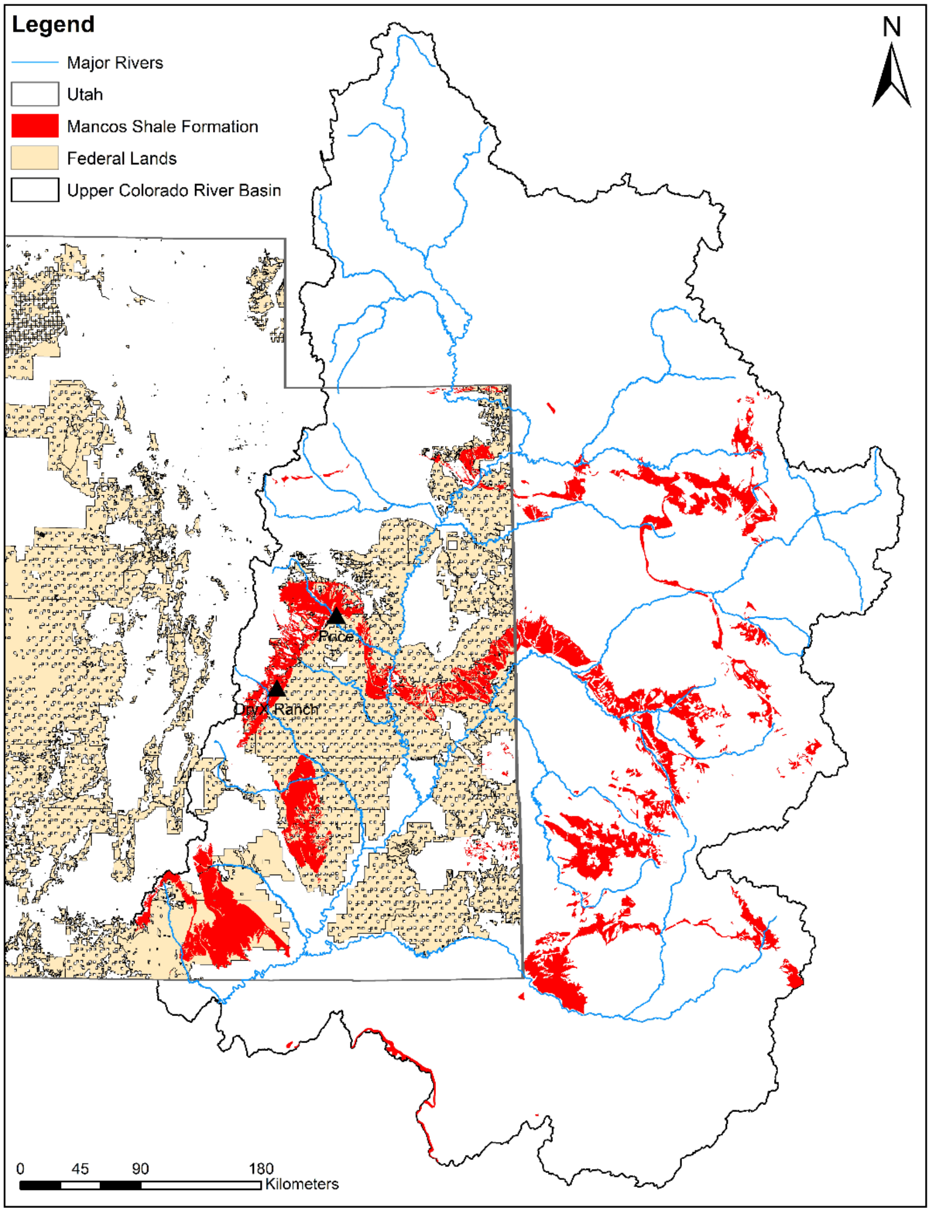

Figure 2: Geographic map of the extent of the Mancos Shale formation in the UCRB and its extent within Utah lands under the control of the BLM/BoR.

In light of this, the Bureau of Land Management (BLM), U.S. Department of Agriculture - Agricultural Research Service, Bureau of Reclamation (BoR), and Desert Research Institute are investigating sediment and salinity contributions to the Colorado River from saline and sodic soils of rangelands in the Colorado Plateau. There are two goals for this project: (1) improve the understanding of sources and transport mechanisms of salinity and sediment loads into streams from rainfall-induced runoff within the UCRB and (2) parameterize our findings so they can be implemented into the Rangeland Hydrology Erosion Model (RHEM). This study describes field experiments, laboratory analyses, and numerical simulations conducted to investigate salinity and sediment loading in response to the quantity and spatial distribution of vegetation canopy cover (VCC) on varying slope, geology, and rainfall intensity on rangelands in the vicinity of Price, Utah. Our findings will allow RHEM to be used as a tool to aid land management decisions that address sediment and salinity loads in the Colorado River.

2 Research Objectives and Hypotheses

The research objectives of this project are to investigate: (1) if a linear relationship between sediment erosion and salinity loading in runoff exists for the Mancos Shale and if this relationship can be used in RHEM to predict salinity and (2) determine what ameliorating effect vegetation amount and spatial pattern has on runoff sediment and salinity. We hypothesize that:

1. Sediment and salinity loading processes during an erosion event have a linear relationship.

2. The amount and spatial pattern of vegetation has a significant influence on salinity and sediment loading in runoff during a rainfall event due to reduced splash and sheet erosion, increased infiltration, and reduced flow velocity.

Our analysis will improve parameterization of the RHEM model for estimating the erosion of saline and sodic soils of the Colorado Plateau under different rainfall scenarios.

3 Background and Literature Review

This section gives detailed background information that is pertinent to understand the purpose of this research. In order to understand the ameliorating effect the amount of vegetation and spatial pattern has on sediment erosion and salinity transport processes, we must establish an understanding of:

- The geologic history of the Mancos Shale formation because the depositional environments in which the Mancos Shale formation developed (e.g. parent material) influences the variability in soil geochemistry at a given location. In addition, soil chemistry, as well as climate and topography, influences what vegetation (if any) is present.
- The Price River Basin salinity because the Price River contributes a substantial portion of salinity to the total salinity load of the Colorado River.
- Sediment erosion and salinity transport processes because these are the two processes we hope to manipulate through vegetation.
- Vegetation effects on soil and erosion processes because the BLM/BoR hopes to use vegetation on highly erodible hillslopes to decrease sediment and salinity loading into the Colorado River.
- Landscape pattern descriptions because we want to evaluate if the spatial distribution of VCC has a measurable effect on sediment erosion and salinity transport processes.

- The Rangeland Hydrology and Erosion Model because it is the mechanistic model we use in this study and it’s the model the BLM/BoR are interested in using as a land management tool.

3.1 Geologic history of the Mancos Shale formation

Hettinger and Kirschbaum [2002] summarize the geologic history and lithology of the Mancos Shale Formation. During the Late Cretaceous (95 - 67 Ma) the Uinta Basin region was located near the Western Interior Seaway and within the Cretaceous Rocky Mountain Foreland basin. Fluvial systems transported sediment eastward from the Sevier highlands to the coastal areas and coal-forming wetlands occupying the coastal plains. When the seaway reached its maximum extent, the western shoreline was located in Central Utah during the Turonian age. Between the Turonian age and the early Campanian age, the shoreline began to slowly retreat. During the Campanian age, the shoreline repeatedly migrated back and forth until it permanently moved out of the region during the Maastrichtian age [Hettinger and Kirschbaum, 2002]. As a result, the Mancos Shale is dominated by mudrock that accumulated in offshore, shallow, open marine environments within the Cretaceous Interior seaway and therefore contain high quantities of salts. The Mancos Shale is between 95 - 80 Ma, contains five members, and is part of the Capital Reef Stratigraphy. First, the Tununk member contains fossil rich, silicified bluish gray shale inter-bedded with mudstone, fine-grained sandstone, and siltstone. Next, the Ferron Sandstone was deposited in a wave-dominated delta and river system and contains brown fine-grained sandstone and white cross-bedded sandstone with inter-bedded gray shale rich in carbonates and known to have coal and oil deposits. The Blue Gate member resembles the Tununk member, is light gray to bluish gray, and contains bentonite-rich clays, shaly siltstone, and sandstone. The Muley Canyon member contains bedded, fine-grained sandstone and carbon-rich shales known to have coal deposits. Finally, the Masuk member resembles the Blue Gate member and contains cross-bedded sandstones and yellowish-gray to bluish-gray mudstone with inter-bedded light gray sandstone [Weiss et al., 2003; Witkind, 2006; Orkild, 1956]. The Price field site for this study is located within the Tununk member (Figure 3a) and the Ferron field site (a.k.a. Dry-X) is located within the Blue Gate member (Figure 3b) of the Mancos Shale formation, both of which are immediately downslope of the Ferron Sandstone member.

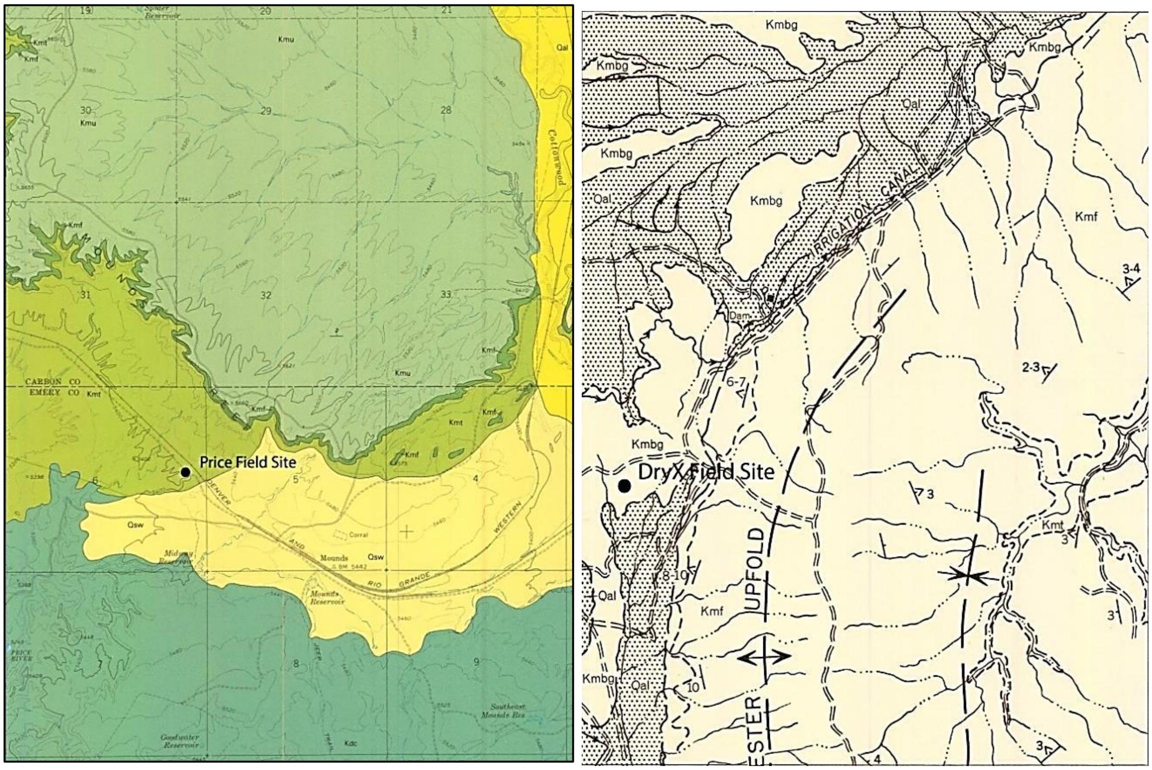

Figure 3a-b: Partial geologic maps of each field site showing their location on a specific geologic member. (a) Partial geologic map of Price field site located on the Tununk Member (Kmt) of the Mancos Shale formation [Witkind et al., 2006]. (b) Partial geologic map of Dry-X field site located on the Blue Gate Member (Kmbg) of the Mancos Shale formation [Orkild, 1956].

3.2 Price River Basin Salinity

The Price River Basin is subject to runoff-producing spring snowmelt and summer precipitation occurring as high intensity, short duration, convectional storms. Salinity loading mainly occurs during the summer months and is most pronounced after the first storm [Lin et al., 1984] of the season. Surface water salinity is controlled by salt concentration and salt transport that is related to soil erosion processes [Bauch and

Spahr, 1998]. Natural salinity loading occurs predominantly from surface runoff and erosion processes from these summer storms on steep, incised Mancos Shale slopes [Lin et al., 1984]. Rao et al. [1984] found that the dominant salt species in the Mancos Shale formation are alkaline earth carbonates and sulfates. These are soluble and easily transported as dissolved solids in water or in some cases, hydraulic lift. After long dry periods, initial summer storms allow salts to accumulate on the surface as salt efflorescence (thenardite, Na_2SO_4; also possibly gypsum). Efflorescence crust forms from the upward flux of saline soil water and accumulates within approximately the first ten days after a storm event. The formation of efflorescence crust is inhibited by the lack of water in the soil or crust formation itself that cuts off vapor flow shortly after this ten day period. For each storm that occurs afterward, the magnitude of salinity loading tends to decrease and may be dependent on the duration of the dry period after the storm event [Rao et al., 1984]. It is estimated that approximately 7.5 - 8.5% of the total salinity loading in the Price River Basin comes from salt efflorescence [Bowles et al., 1982]. Salt efflorescence is most commonly found in low lying areas like stream channel beds and rills. During flash floods, these ephemeral channels in arid and semiarid regions can be highly efficient at transporting salt laden sediments [Laronne and Reid, 1993; Reid et al., 1996]. Rill development and ephemeral channel erosion drives sediment transport [White and Hawkins, 1980; Shen, 1981; Jackson et. al. 1984], while significant salt transport occurs in concentrated flow erosion and is often exacerbated by the presence of salt efflorescence [Riley et al., 1982].

3.3 Sediment Erosion and Salinity Transport Processes

Water driven sediment erosion processes occur in three phases: (1) soil particles detach from the surface from raindrop impact; (2) detached particles are transported by overland flow downslope (generally unidirectional); and (3) as water velocity decreases, deposition of particles occurs [Breshears et al., 2003]. Differences of water erosion and sediment transport occur from several factors: (1) precipitation distribution; (2) vegetation canopy cover; and (3) soil moisture and soil texture [Breshears et al., 2003]. In inter-rill areas, soil particle detachment occurs by raindrop impact and these detached soil particles are transported by overland flow. As the depths of overland flow downslope increases, overland flow protects the ground surface from raindrop impact, varying inversely with slope length [Abrahams et al., 1991]. Laronne and Shen [1982] conducted a study on the Mancos Shale and determined that several factors of solute pickup are related to sediment erosion processes and include: (1) precipitation and initial runoff being under-saturated with respect to soil minerals, (2) slope, (3) runoff rate, (4) rill development, and (5) dissolution of transported sediment particles. In addition, Ponce [1975] showed statistically significant linear correlations between salinity and sediment in runoff on individual rainfall plots from several geologic members of the Mancos Shale formation. Ponce [1975] attributed the variability in the linear correlations to the variability in dissolution rates of suspended sediment particles.

In addition, Evangelou [1981] showed that when high concentrations of Ca^{2+} is present in runoff, the release of ions (primarily Na^{+} and Mg^{2+}) on the Mancos Shale is directly related to and regulated by the exchange complex, represented as the cation exchange capacity (CEC), and the relative cation adsorption affinities of the soil minerals. Therefore, CEC is the mechanism that drives a substantial increase in salinity loading on Mancos Shale soils.

Microphytic crusts also have an effect on runoff, soil erosion, and salt transport, depending on their level of development and disturbance [Belnap et al., 2013]. Biological soil crusts (microphytic crusts) are typically erosion resistant and affect infiltration rates by blocking flow through macropores and bridging erodible soil particles into erosion resistant soil aggregates [Eldridge, 1998]. They also can enhance porosity and infiltration by increasing aggregates and surface roughness [Loope and Gifford, 1972; West, 1991; Eldridge, 1993]. Areas where microphytic crusts have no trampling to moderate trampling rates from animals typically have a high degree of stability and lower erodibility. Conversely, if the trampling rate is high, soil erodibility increases [Eldridge, 1998]. The majority of research has shown that intact microphytic crusts reduce soil erosion and soil detachment, but the role of microphytic crusts in altering transport of salts is poorly understood [Belnap, 2006].

3.4 Vegetation Effects on Soil and Erosion Processes

Infiltration rates are controlled by vegetation, soil properties, climate, and topography [Wood and Blackburn, 1981]. In arid and semi-arid landscapes, the amount of runoff and infiltration may be a function of vegetation patterns [Chartier et al., 2011]. Loch [2000] found that infiltration totals and rates increased with increasing vegetation cover. In general, soil beneath the canopy acts as a sink for water, sediment, and nutrients, whereas interspace (bare soil) areas act as a source [Howes and Abrahams, 2003]. Charley and West [1975] found distinct soil chemical patterns of carbon, nitrogen, phosphorus, pH, and salinity vertically and horizontally between vegetation and bare soil areas. In addition, Zucca et al. [2011] found an increase in soil nutrients, ions, CEC, and sodium absorption ratio (SAR) under the canopy of *Atriplex nummularia* in Morocco, indicating that vegetation affects the spatial distribution of these soil properties. VCC can have a large effect on water erosion and runoff processes, primarily because of rainfall interception [Wischmeier and Smith, 1978]. Carroll et al. [2000] found that as VCC increases, there is a reduction in both runoff electrical conductivity (EC) and sediment loss on varying slopes. Bartley et al. [2006] conducted a hillslope-scale study on savanna rangelands in Australia and found that even with high mean VCC, small patches of interspace had 6-9 times more runoff and 60 times more sediment loss than similar hillslopes that did not contain as much or any interspace patches. In addition, the sediment load consisted of fine suspended load rather than coarse bedload material and the majority of soil loss occurred during the initial runoff event. Furthermore, Bartley et al. [2006] highlight the importance of having medium to high VCC patches at the bottom of hillslopes so vegetation may trap and store sediment, thereby reducing sediment entering the stream network.

Interception of rainfall by vegetation is a function of precipitation and canopy characteristics [Hamilton and Row, 1949; Slatyer, 1965; Navar and Bryan, 1990; Domingo et. al., 1994]. Interception reduces runoff volumes, and stemflow may promote deep infiltration into the soil directly beneath the canopy [Branson et al., 1972]. In most cases at the beginning of a rainfall event, canopies efficiently intercept almost all rainfall within the area they project over the ground until a maximum is reached when the cumulative interception is equal to the amount of precipitation. Some rainfall makes it through the canopy and reaches the surface as through-fall. Once the maximum cumulative interception threshold is exceeded, rainfall water captured by the canopy may make its way to the soil below via foliar drip and stemflow. The amount of time to reach maximum cumulative interception is dependent upon the type of plant and the rainfall intensity [Wood et al., 1998]. Proportionally, rainfall lost to vegetation interception is most significant under conditions of lower rainfall intensities and may strongly influence erosion rates under such conditions [Simanton et al., 1991].

Vegetation-driven spatial heterogeneity (VDSH) explains how soil development and evolution processes relate to vegetation versus interspace areas [Puigdefabregas, 2005]. Rills and gullies are considered erodible sediment conveyors, transporting detached sediment downslope as concentrated flow, depending on VDSH and the detachment and conveyance hydraulic factors. VDSH influences sheet runoff and concentrated flow processes possibly by creating obstacles which increases the tortuosity of concentrated flow paths and reduces flow velocity. This in turn may influence rill and channel development and affect salinity and sediment loading along these flow paths [Wilcox et al., 1996; Davenport et. al., 1998; Urgeghe et al., 2010; Weltz et al., 2014]. When vegetation becomes sparse runoff tends to concentrate in narrow channels whereas when vegetation becomes dense runoff channels widen. This differential response seems to reflect the existence of a channel network characterized by VDSH [Puigdefabregas, 2005; Al-Hamdan et al., 2012].

3.5 Pattern Descriptions

Landscape ecology involves the study of landscape patterns at a variety of scales to quantify the interactions among patches within a landscape mosaic and how these patterns and interactions change with time. Landscape patterns, when quantified, allow for the study of landscape function and change [McGarigal and Marks, 1995]. In this study, landscape pattern metrics are used to quantify VCC and soil interspace patterns and to investigate their relationship to erosion and salinity. There are three levels of landscape pattern metrics: landscape, class, and patch. Fragstats is a program designed to compute a variety of pattern metrics for categorical map patterns for all three levels. As described by McGarigal [2015]:

> "Landscape metrics measure the aggregate properties of the entire patch mosaic (p. 84). Class metrics measure the aggregate properties of the patches belonging to a single land cover type (p. 82). There are two basic types of metrics at the class level: (1) indices of the amount and spatial configuration of the class, and (2) distribution statistics that provide first- and second-order statistical summaries of the patch metrics for the focal class (p. 82)."

Both landscape and class metrics share the same distribution statistics that include: mean (MN), area-weighted mean (AM), median (MD), range (RA), standard deviation (SD), coefficient of variation (CV). Each level of landscape pattern metric has associated with it a series of specific pattern metrics: area-edge, shape, core area, contrast, aggregation, and diversity. Area-edge metrics are metrics that deal with the size of patches and the amount of edge created by these patches [McGarigal, 2015]. Area metrics quantify landscape composition, whereas edge metrics quantify non-spatially explicit landscape configuration [McGarigal and Marks, 1995]. Shape metrics describe landscape configuration [McGarigal and Marks, 1995] by the interaction of patch shape and size and its complexity [McGarigal, 2015]. Contrast metrics describe the magnitude of difference between adjacent patch types with respect to one or more attributes at a given scale that are relevant to the process under consideration [McGarigal, 2015]. Aggregation metrics describe the tendency of patch types to be spatially aggregated or “contagious” distributions (i.e. landscape texture). Aggregation metrics describe four types of concepts: (1) dispersion, (2) interdispersion, (3), subdivision, and (4) isolation. Dispersion describes how spread out or dispersed a patch type is. Interdispersion describes with how often multiple class types spatially intermix. Subdivision describes how patch types are broken up into separate patches. Isolation describes the degree to which patches are spatially isolated from one another by distance [McGarigal, 2015].

3.6 Rangeland Hydrology and Erosion Model and its Application

The Rangeland Hydrology and Erosion Model (RHEM; Nearing et al. [2011]) is a process-based model that was used in this study to investigate how the amount and spatial distribution of VCC affects sediment and salinity loading in runoff during a rainfall event. The RHEM model simulates hillslope runoff and erosion responses based on two process model components within the core engine. The hydrology component of the RHEM model is based on the KINEROS2 (K2) model that incorporates infiltration and overland flow [Smith et al., 1995]. The erosion component of RHEM incorporates concentrated flow [Foster, 1982] and splash and sheet flow [Wei et al., 2009] to simulate soil erosion [Al-Hamdan et al., 2015]. The current version of RHEM (2.3) is set up so that Kss (splash and sheet erodibility coefficient) is the primary indicator of erosion while Kw (undisturbed concentrated flow erodibility coefficient) is the primary indicator of transport of the eroded sediments [M. Hernandez, USDA, pers. Comm. 2015]. RHEM was set up this way because it is assumed that sediment detachment is dominated by splash and sheet erosion while the major role of concentrated flow paths is transporting the sediments detached by splash and sheet flow. Currently, RHEM doesn’t model salinity chemistry and transport processes. However, in this research, we hope that with an improved understanding of the relationship between suspended sediment and salinity loading in runoff we can use the sediment output of the model as a proxy to estimate an associated salinity output.

4 Methods

Methods were designed to collect information on: (1) the amount and spatial distribution of VCC; (2) micro-topography; (3) runoff flow rates, quantity and chemistry; (5) sediment quantity; and (6) soil chemistry variability with depth and between vegetation versus interspace. Measurements were made under four rainfall intensities on varying slope, geology, and VCC to quantify how VCC influences sediment and salinity loading on rangelands saline and sodic soils.

4.1 Field Methods

4.1.1 Site Description

The Price region of Utah (Figure 4) has an arid climate influenced by summer monsoonal convectional thunderstorms and contains a salt desert shrubland ecosystem. The study sites are located in the Price-San Rafael River Basin (1.1×10^4 km^2). The city of Price, Utah has a mean annual precipitation of 233 mm/yr and mean air temperature of 10 °C, over the 1968 - 2014 period [Western Regional Climate Center, 2014]. The Price field site (110° 36' 26" W, 39° 27' 47" N; Figure 5a) is located within the Tununk member of the Mancos Shale formation 23 km SE of the city of Price at an elevation of 1700 m ASL. Price contains well developed, light gray soil crusts containing sparse VCC (3.3% - 17.8%)

on shallow grade slopes (0.7% - 10%). The soil series found at Price is the Persayo loam [USDA-NRCS, 2013]. The vegetation at the site is comprised of halophytes and salt-tolerant vegetation that include a mixture of four shrubs (*Krascheninnikovia lanata*, *Chrysothamnus nauseosus*, *Atriplex gardneri*, *Ephedra viridis*), two subshrubs (*Eriogonum microthecum* and *Helianthella microcephala*), and three grass species (*Achnatherum hymenoides*, *Hilaria jamesii*, *Elymus elymoides*). The most predominant plant species were *Atriplex gardneri*, *Ephedra viridis*, and *Achnatherum hymenoides*. The Dry-X field site (111° 7' 21" W, 38° 58' 23" N; Figure 5b) is located within the Blue Gate member 74 km SSW of Price at an elevation of 1900 m ASL. Dry-X contains poorly developed, light-medium gray soil crusts with moderate VCC (17.7% - 26.4%) on moderately steep slopes (11.4% - 24.5%). The soil series found at Dry-X is the Chipeta-Badland complex [USDA-NRCS, 2013]. The vegetation at the site is solely comprised of the salt-tolerant halophyte shrub species, *Atriplex corrugata*. Both sites contained a marginal amount of cattle and antelope hoof impressions in the soil.

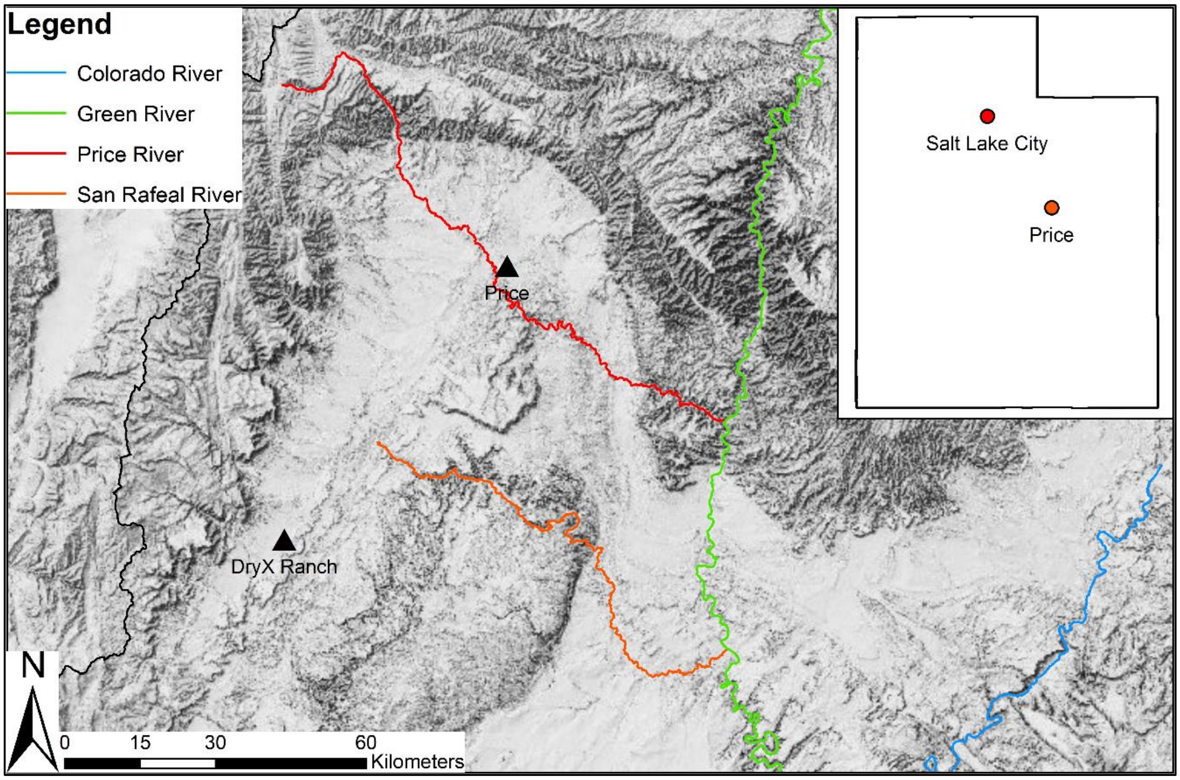

Figure 4: Geographic map of the field sites relative to rivers in the Upper Colorado River Basin.

Figure 5a-b: Photos from Price (a) and Dry-X (b) field sites.

4.1.2 Plot Selection and Installation

The Price and Dry-X sites were selected because of their location on the Mancos Shale formation, varying vegetation cover and slope, accessibility for field work operations, and National Environmental Policy Act (NEPA) clearance. At the Price and Dry-X field sites, 6x2 m rainfall simulation plots were installed. The locations of each plot on the hillside were placed where rills were already developed that would carry water down-gradient. Once the location of each plot was determined, a Nikon NPR 352 total station was used to make the plot borders equal-diagonal (square) to one another. After making the plots square, metal stakes and construction string indicated where the 2x0.2 m steel plates were installed on the top and side borders. At the bottom of the plot, a flume was installed to channel runoff from the plot into the runoff collection pit. At each site, there were 5 types of plots: (1) control (no rainfall), (2) 2 year storm, (3) 10 year storm, (4) 25 year storm, and (5) 50 year storm. Separate plots were established for three replications of each rainfall intensity. The control plots were only used for a prior characterization of soils and were not replicated. The number of replications was chosen as a balance between available resources and the statistical validity of results.

4.1.3 Rainfall simulation

The study used a custom-modified Walnut Gulch rainfall simulator (WGRS) that completely and evenly covered the 6x2 m plots (Figure 6) [Paige et al., 2004]. The simulator has a central oscillating boom that is 6.1 m long with a 5 cm internal diameter. The oscillating boom is controlled by a high-torque stepper motor with a chain and gear sprocket system. The central boom has four VeeJet 80100 nozzles spaced 1.52 m apart that sit 2.44 m above the plot. The spray produced by the nozzle is a long, narrow oval approximately 2.8 m long. The boom is supported by three sets of telescoping 4.6 m legs that can be adjusted by 5 cm increments to a maximum boom height of 3.3 m. Metal crossbars are attached to the legs for additional stability. On the top and sides of the simulator are windbreaks to minimize the effects of wind on the distribution of rainfall across the plot. Nozzle spray is controlled by a pressure regulator that maintains a constant nozzle pressure of 55 kPa. Rainfall intensity (a function of the amount of time the nozzles are operating) is controlled by changing the length of time between oscillations and the activation of individual nozzles. The oscillating boom and its components are computer controlled [Paige et al., 2004].

Intensities for our rainfall simulations were determined from the NOAA Atlas14 point precipitation frequency estimates for the Price area where our field sites were located. Based on 5 minute rainfall amounts derived from the Atlas14 database [http://www.nws.noaa.gov/oh/hdsc/index.html], four rainfall intensities were applied:

(1) 50.8 mm/hr, (2) 88.9 mm/hr, (3) 114.3 mm/hr, and (4) 139.7 mm/hr. Water that was used during the rainfall simulations was obtained from the firehouse station at the BLM Price office. The WGRS was connected to a Husky 1000 gal (3785 L) self-supporting onion tank using a series of water hoses and pumps.

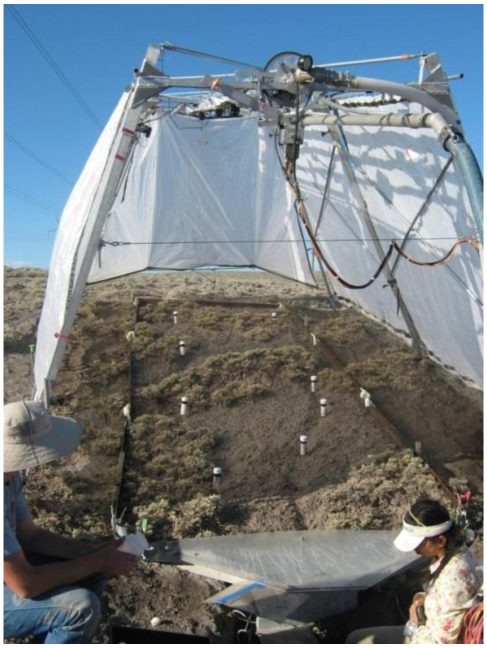

Figure 6: Walnut Gulch rainfall simulator operating at Dry-X.

4.1.4 Runoff Sampling

Runoff was collected during each simulation using two different collection containers. Runoff water chemistry samples were collected using VWR 50 mL centrifuge tubes and runoff sediment samples were collected using 1 L Nalgene bottles, neither of which was pretreated. The same runoff sampling protocol was applied to each field site with the exception of the timing intervals when runoff was collected. On the first field expedition to the Price site, 10 rainfall simulations were completed. On that trip, runoff was collected every 30 seconds for the first 9 minutes, and after the 9th minute, runoff was collected every minute until the end of the rainfall simulation. On our second field expedition for two additional plots at Price and 12 plots at Dry-X, runoff was collected every 30 seconds for the first 3 minutes and then every 3 minutes until the end of the rainfall simulation. The protocol was changed because rainfall simulations from the first field expedition did not appear to have been run long enough for the hydrograph discharge to consistently reach steady-state. One water chemistry sample was collected in a VWR 50 mL centrifuge tube from the Husky water tank containing the water that is applied during a rainfall simulation before each rainfall simulation occurred. The runoff sediment samples were stored without refrigeration in plastic crates. The runoff water chemistry samples were covered with para-film around the cap to reduce the chance of leakage and placed in large plastic Ziploc bags that were labeled with the plot identification number and stored inside coolers with dry ice in order to reduce subsequent bacterial chemical reactions. By the end of our field work, we had collected a total of 473 runoff water quality samples (includes 24 applied rainfall water chemistry samples); 275 came from Price and 198 came from Dry-X. In addition, we collected a total of 263 runoff sediment samples; 133 came from Price and 130 came from Dry-X.

4.1.5 Soil Sampling

Soil bulk density samples were collected at control plots using the AMS soil sampler with a 5 cm inside diameter, 3 cm long attachment. The pre-rainfall soils were collected on the control plots using a standard hand shovel due to the lack of soil adhesion. The control plots provided information on pre-simulation soil characteristics, since sampling in the rainfall plots would affect the flow and erosion. In the plots where rainfall was applied, post-rainfall soils were collected using an AMS split soil core sampler which is 25 cm long with a 5cm inside diameter. At each plot, soils were collected at three locations under the vegetation canopy and three interspace locations. Soil sample locations were subjectively chosen in an area towards the middle portion of the plot to minimize the lateral flow affects that may occur near the plot borders. Soil cores were then separated by depth increments into the surface crust (0 cm), depth increment 1 (0-5 cm), and depth increment 2 (5-10 cm) (Figure 7). The number of depth increments and the total depth of the core was determined by the depth of the wetting front from the first soil core collected at each plot. Depth increments are included in the sampling protocol because of the possible salt changes with depth that may be mobilized by varying rainfall intensities and VCC. Finally, each soil sample was made into a composite soil sample with respect to vegetation versus interspace and by depth increment, resulting in 6 composite samples per plot. The soil samples were stored in Ziploc bags and placed in a cooler with refrigeration. By the end of our field work, we had collected a total of 198 soil samples (102 from Price and 96 from Dry-X).

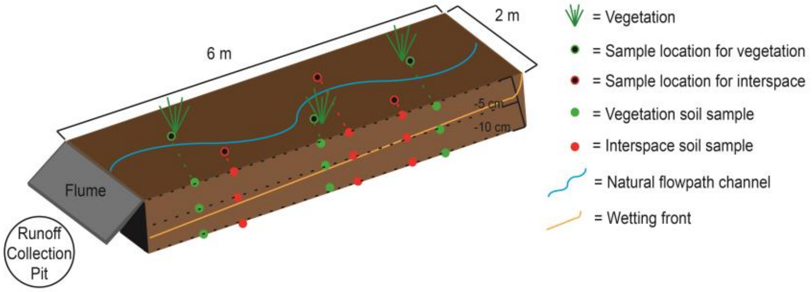

Figure 7: Conceptual drawing of the plot setup and sampling locations for runoff and soil.

4.1.6 Measuring Vegetation Canopy Cover

The distribution of vegetation cover within each plot was mapped using high-resolution photogrammetric models that were developed using Structure from Motion (SFM) 3D reconstruction with numerous handheld digital photographs [Nouwakpo et al., 2015]. Individual 3D points were assessed to determine whether they were part of the vegetation canopy versus soil or surface litter using the following method. A coarse estimation of soil surface topography was created by superimposing a 5 cm grid over the plot and finding the lowest 3D point within each grid cell. A second order polynomial trend surface was fit to these local minima, and points that were more than 20 cm above this trend surface were identified as tall vegetation based on field observations. For remaining points, two tests were applied. First, the slope from each point to each of its neighbors within 2.5 cm was calculated. The maximum slope within each of four directional quadrants was determined, and points were labeled as vegetation if the minimum value of the maximum slope from each quadrant was greater than 20 percent. The strategy of using the minimum of maximum slope in each direction identified protrusions that were not part of the local trend in surface relief. For the second test, a height was interpolated for the location of each point using an inverse-distance weighting of its four nearest neighbors in each directional quadrant that had not yet been identified as vegetation. The point in question was labeled as vegetation if it was more than 2 cm above that interpolated height as this height was found to minimize confusion between surface roughness and vegetation canopy. Minor errors of omission where sharp surface features were labelled as vegetation were manually edited. Irregularly sampled point clouds representing just vegetation were converted into two dimensional map form by superimposing a 2 mm grid and determining which grid cells contained a vegetation point. That fine grid was then aggregated to a 6 cm grid, and these coarser cells were labeled as canopy if more than half the fine-resolution grid cells nested within were labeled as having vegetation. This secondary aggregation helped reduce the effect of over-prediction from labeling a fine-resolution cell as majority-vegetation even if it had just one or two 3D samples within it. Basal, litter, and rock cover percentages were determined from 900 photo interpreted points superimposed on each plot. Vegetation maps created for each plot can be found in the Appendix A (Figures 31 – 42).

4.2 Laboratory Methods

Runoff water chemistry, soil chemistry, soil texture, and soil bulk density samples were processed and measured in the USDA-ARS soils laboratory in Reno, Nevada.

4.2.1 Runoff Water Chemistry

Each sample was centrifuged at 2000 rpm for 3 minutes so the limited sediments inside would settle to the bottom and ions could be measured directly from the water sample in the centrifuge tube. Soluble cations in runoff Ca^{2+} and Mg^{2+} were quantified using atomic absorption spectroscopy and K^+ and Na^+ by atomic emission spectroscopy using a Perkin Elmer Atomic Absorption (AA) Spectrometer. Both Price and Dry-X runoff water chemistry samples required dilution to be within a detectable range on the AA. Ammonium (NH_4^+) was measured using a Lachat Quickchem Flow Injection Analysis+ instrument. Soluble anions (NO_2^-, NO_3^-, SO_4^{2-}, Cl^-) in runoff were measured using a Dionex Ion Chromatograph (IC) with a AS18-4µ column. Price and Dry-X runoff water chemistry samples also required dilution to be within the detectable range of the IC. Ortho-P was below detection limit for nearly all samples. Runoff pH and EC were measured in the lab using an Oakton pH Meter 510 Series and VWR Scientific EC Meter Model 2052, respectively.

4.2.2 Soil Chemistry

Soluble-phase cations and anions were extracted by immiscible displacement (ID) [Mubarak and Olsen, 1977]. Solution-phase anions (NO_2^-, NO_3^-, SO_4^{2-}, Cl^-) were measured using a Dionex Ion Chromatograph (IC) with a AS11-HC column. Some samples very high in SO_4^{2-} and Cl^- required dilution to be within the detectable range of the IC. Solution-phase Ca^{2+} and Mg^{2+} were quantified using atomic absorption spectroscopy and K^+ and Na^+ using atomic emission spectroscopy with a Perkin Elmer Atomic Absorption (AA) Spectrometer. Extractable cations (Ca^{2+}, Mg^{2+}, K^+, Na^+) in soil were extracted using the ammonium acetate (NH_4OAc) method [Thomas, 1982] and quantified using atomic spectroscopy as stated above. Some samples that were very high in Na^+ for some samples required dilution for both ID and NH_4OAc extractions to be within the detectable range of the AA. Soil mineral N (NO_2^-, NO_3^-, NH_4^+) was extracted using 1.5M KCl [Bundy and Meisinger, 1994] and quantified on the Lachat system. Cation exchange capacity (CEC) was measured according to methods of Bower et al. [1952]. Soil solution-phase ion solution produced by ID was measured for pH and EC using an Oakton pH Meter 510 Series and VWR Scientific EC Meter Model 2052, respectively.

4.2.3 Soil Texture, Bulk Density, and Porosity

Soil texture was measured using methods of Jackson and Barak [2005] on the pre-rainfall soils of the control plots. Soil bulk density was calculated by measuring the dry weight of the soil samples in the lab and using the following equation:

$$\rho_b = \frac{m_s}{V} \qquad (1)$$

where m_s is the mass of dry soil (g/cm^3) in volume V. Soil porosity (φ) was determined using the following equations from Jury and Horton [2004] that relates bulk density to soil porosity:

$$\frac{m_s}{V} = \frac{m_s}{V_s}\frac{V_s}{V} \qquad (2)$$

where m_s is the mass of dry soil (g/cm^3) in V. Thus, $\rho_b = \frac{m_s}{V}$ and $1 - \varphi = \frac{V_s}{V}$, then:

$$\rho_b = \rho_s(1 - \varphi) \qquad (3)$$

4.3 Data Analysis

4.3.1 Data Processing

All runoff water chemistry and soil sample ion concentrations (mg/L) measured in the laboratory were also converted to milliequivalents/liter (meq/L). All runoff data time stamps were identified and organized to match the runoff water chemistry samples with runoff sediment samples. In addition, total dissolved solids (TDS) was calculated for the blank sample of water applied during the rainfall simulation for each plot, and this initial value was subtracted from the TDS for each runoff water quality sample. For ID treated soils data, soil SAR was calculated each soil sample using the following equation:

$$SAR = \frac{Na^{+}}{\sqrt{\frac{1}{2}(Ca^{2+} + Mg^{2+})}} \qquad (4)$$

where Na^{+} is the soil sample sodium concentration, Ca^{2+} is the soil sample calcium concentration, and Mg^{2+} is the soil sample magnesium concentration; all concentrations are in meq/L.

4.3.2 Differences between the Tununk and Blue Gate members

Principal component analysis, a multivariate statistical method used to take a large dataset and identify a smaller number of uncorrelated variables, was used to visualize the variability between Price and Dry-X runoff water and soil chemistry ions from ID and ascertain if they have inherently different runoff water and soil ion chemistry. Score plots of the first and second components and tables showing the coefficients for each ion were created for both runoff water and soil chemistry PCA results.

The average TDS, sediment, soil SAR, and soil CEC was calculated for each plot. Boxplots were used to assess if there are substantial differences between the Price and Dry-X means for runoff TDS (mg/L), sediment concentration (kg/L), soil SAR, and soil CEC (cmol+/kg).

4.3.3 Relationship between Sediment and TDS

Reduced major axis (RMA; type II) linear regression analysis was done for sediment concentration (kg/L) versus salinity concentration (TDS; mg/L) in runoff in order to investigate if there is a linear relationship between suspended sediment and salinity and if sediment concentration can be used as a proxy for salinity concentration when using the RHEM model. Average TDS and sediment concentrations were calculated for each respective plot. RMA regression was used since there was relatively significant unexplained error in our predictor variable (sediment concentration) that ordinary least squares (OLS) regression cannot adjust (OLS assumes no error in predictor variable) for resulting in a biased regression model which in our case, would provide erroneous results. Reduced major axis regression makes no assumptions about dependence [Friedman et al., 2013] and minimizes the sum of triangular areas between data points and the best fit line [Carr, 2012]. R^2_{Pred}, a leave one out validation statistic, was used to evaluate if the regression model provides valid predictions. If the difference between R^2 and R^2_{Pred} is > 0.1, this indicates the model over-fits the data and isn't suitable for calculating accurate predictions [Myers et al., 2012].

4.3.4 RHEM Calibration

Iterative parameter optimizations were performed to select proper estimates for RHEM sediment- and discharge-related parameters using the multi-objective complex (MOCOM) global optimization method by Yapo et al. [1998]. McGwire et al. [2011] describe MOCOM as incorporating the benefits of a controlled random search, competitive evolution, Pareto ranking, and a multi-objective downhill simplex search. MOCOM calculates a set of Pareto optimal solutions that show the tradeoffs between multiple objective measures. MOCOM adjusts the selected model parameters using N simplexes with randomized parameter values until it reaches a set of solutions that represent the tradeoffs between the objective functions of the root mean square error (RMSE) and absolute percent bias (|%Bias|). These objective functions were calculated using the following equations:

$$RMSE = \sqrt{\frac{\sum_{i=1}^{n}(O_i - P_i)^{\,2}}{n}} \qquad (5)$$

$$|\%Bias| = \left|\frac{\sum_{i=1}^{n}(O_i - P_i) * 100}{\sum_{i=1}^{n}(O_i)}\right| \qquad (6)$$

Where n is the number of the plot, O_i is the observed ith plot to be evaluated, and P_i is the simulated value by the model for the corresponding ith plot. For this study, we subjectively chose a solution that had relatively low RMSE within a range of solutions that were effectively unbiased. Before calibrations began, background literature on the RHEM model was reviewed to find any input parameters that had a well-defined reference value. Gw (capillary drive) was the only parameter found in the literature that had a well-known literature value established for the soils encountered in this study and likely wouldn't be affected by the saline and sodic soils encountered in this study. The KINEROS2 documentation [Smith et al., 1995] established a mean of 200mm for silt loam soils, thus we used this value for both sites as the default value. The default input parameters are found in Table 1. For detailed input parameter descriptions, see Appendix B.

Table 1: Default input parameters used in the calibration for both sites.

Input Parameters	Description	Default Values
CLEN	hillshope length (m)	30
DIAMS	soil particle diameters (mm)	0.002, 0.01, 0.03, 0.2, 0.3
DENSITY	particle densities (g/cc)	2.60, 2.65, 1.80, 1.60, 2.65
LEN	plot slope length (m)	6
WIDTH	plot slope width (m)	2
SX	normalized distance	1
CV	Ke coefficient of variation	1
IN	interception depth (mm)	1
G (i.e. Gw)	mean capillary drive (mm)	200
DIST	pore size distribution	0.23
SMAX	upper limit to saturation	1
ADF	Beta decay factor	0
RSP	rill spacing (m)	1
SPACING	average micro-topographic spacing (m)	1

Several input parameters were directly estimated for each plot. Chezy coefficients ($m^{1/2}$ s^{-1}) for overland and concentrated flow were estimated using a modified equation from Crowe et al. [2009]:

$$Chezy = \sqrt{\frac{8g}{f_t}} \qquad (7)$$

where g is the acceleration of gravity ($m\ s^{-2}$) and f_t is the Darcy-Weisbach friction factor estimated by Al-Hamdan et al. [2013]:

$$f_t = 10^{-0.109+1.425litter+0.442rock+1.764(basal+crypto)+2.068S} \qquad (8)$$

where *litter* is the fraction of area covered by litter to total area, *rock* is the fraction of area covered by rock to total area, *basal* is the fraction of area covered by basal canopy to total area, *crypto* is the fraction of area covered by cryptograms (i.e. biological soil crust) to total area, and *S* is percent slope. Based on RHEM [2015], the splash and sheet erosion erodibility coefficient, Kss, was estimated as:

$$K_{ss} = 10^{4.2587-2.547G-0.7822F+2.5535S} \quad \text{if G} < 0.475 \qquad (9)$$

where *G* (ground cover) is the fraction of area covered by plant basal area plus litter area to total area, *F* is the fraction of area covered by canopy to total area, and *S* is slope. G was less than 0.475 for all plots in both field locations. The undisturbed concentrated flow erodibility coefficient (s^2 m^{-2}), $K\omega$, is calculated as [Al-Hamdan et al., 2015]:

$$K_{\omega} = \ 10^{-4.14-1.28basal-0.98rock-15.16clay+7.09silt} \qquad (10)$$

where *basal* is the fraction of area covered by basal canopy to total area, *clay* and *silt* are the fractions of the site's soil texture. The effective hydraulic conductivity (mm h^{-1}), Ke, was calculated using the following equations [RHEM, 2015]:

$$K_{eb} = 1.2exp^{2.0149(basal+litter)} \qquad (11)$$

$$K_e = K_{eb} * 1.2 \qquad (12)$$

Equations 11 and 12 are specifically used to estimate Ke for silt loam textured soils. A summary of the estimated input parameters used in RHEM are in Table 2. For detailed input parameter descriptions, see Appendix B.

Table 2: Estimated input parameters calculated from field observations and empirical equations.

Site	POR	FRACT	Plot	SL	CHEZY	KSS	KOMEGA	CA	KE	ROCK	BARE	LITTER	BASAL
Price	0.447	Clay 0.162	1	0.059	8.628	20950	0.026	0.079	1.469	0	0.921	0.007	0.002
			2	0.048	8.489	17659	0.025	0.059	1.545	0	0.941	0.032	0.003
		Finer silt 0.355	3	0.007	9.562	13263	0.025	0.109	1.52	0	0.891	0.02	0.007
			4	0.059	8.315	16734	0.025	0.113	1.556	0	0.887	0.029	0.01
		Coarser silt 0.355	5	0.067	8.117	17111	0.025	0.119	1.564	0	0.881	0.032	0.009
			6	0.057	8.416	14020	0.025	0.178	1.582	0	0.822	0.024	0.022
		Fine sand 0.064	7	0.066	8.026	17008	0.024	0.08	1.6	0	0.92	0.041	0.011
			8	0.1	7.69	24628	0.026	0.072	1.518	0.002	0.928	0.017	0.01
		Medium sand 0.064	9	0.094	7.835	25142	0.026	0.064	1.496	0.002	0.936	0.014	0.005
			10	0.075	8.128	21748	0.025	0.049	1.526	0.002	0.951	0.02	0.009
			11	0.03	9.115	16894	0.026	0.057	1.514	0.003	0.943	0.015	0.01
Dry-X	0.403	Clay 0.231	1	0.169	6.213	19149	0.002	0.206	1.75	0.01	0.794	0.045	0.052
			2	0.114	7.194	14614	0.002	0.198	1.728	0.007	0.802	0.036	0.055
		Finer silt 0.346	3	0.185	6.186	28252	0.002	0.18	1.607	0.005	0.82	0.026	0.028
			4	0.201	5.928	29548	0.002	0.183	1.631	0.003	0.817	0.03	0.032
		Coarser silt 0.346	5	0.214	5.691	24141	0.002	0.24	1.736	0	0.76	0.035	0.058
			6	0.183	5.932	17289	0.002	0.242	1.823	0	0.758	0.056	0.061
		Fine sand 0.0386	7	0.2	5.985	26454	0.002	0.223	1.65	0	0.777	0.026	0.042
			8	0.187	6.128	24449	0.002	0.177	1.7	0.002	0.823	0.029	0.053
		Medium sand 0.0386	9	0.245	5.408	36656	0.002	0.264	1.575	0.003	0.736	0.021	0.024
			10	0.206	5.764	26909	0.002	0.252	1.633	0	0.748	0.039	0.023
			11	0.184	6.226	25663	0.002	0.243	1.594	0	0.757	0.025	0.025
			12	0.19	6.078	28022	0.002	0.202	1.606	0	0.798	0	0.024

Once the input parameter files were populated, some RHEM input parameters were calibrated to match field-measured values of discharge and sediment. First, RHEM discharge was calibrated by calibrating three parameters that dealt with infiltration and runoff: SAT (initial degree of soil saturation), Ke, and ALF (α fitting parameter). Ke was calibrated using a coefficient (explanation two paragraphs down) that was applied to the following equation for shrub dominated soils:

$$K_e = C_e * (K_{eb} * 1.2) \qquad (13)$$

Where C_e is the calibrated coefficient. Lastly, for ALF, the KINEROS2 documentation [Smith et al., 1995] states ALF = 0.85 for most soils, but since RHEM has never been calibrated for saline and sodic soils before, we calibrated ALF with a wide range that would use the Smith and Parlange [1978] model. Once an optimized solution was found for each site for RHEM discharge, we calibrated the model to find a set of optimized solutions with respect to sediment for each site by calibrating two parameters, Kss and Kw, with a coefficient using the following equations:

$$K_{ss} = C_{ss} * (10^{4.2587-2.547G-0.7822F+2.5535S}) \qquad (14)$$

$$K_{\omega} = C_{\omega} * \left(10^{-4.14-1.28basal-0.98rock-15.16clay+7.09silt}\right) \qquad (15)$$

Where C_{ss} and C_{ω} are the calibrated coefficients.

It is important to note three things. First, Kss, $K\omega$, and Ke were calibrated using a coefficient instead of calibrating the individual coefficients within each individual equation because RHEM hasn’t been calibrated for saline and sodic soils and therefore, we don’t have any comparable studies on similar soils to compare with. By using a coefficient applied to a set of equations to simplify the calibration, we can garner a general sense of how these soils behave differently in comparison to non-saline and sodic soils. Second, the RHEM discharge output has units of mm. A one dimensional discharge measure are in these units because RHEM modeled the volume of discharge over the plot area (12 m^2) giving us a total amount of discharge depth in mm over the plot area. Third, Price plot 12 was initially included in the first round of RHEM discharge calibrations, but a plot of the residuals versus observed (Figure 8) showed that the model wasn’t handling the plot-plot variability because Price plot 12 was an outlier (> 3SD) and the residuals were not random with an upward trend. In result, Price plot 12 was excluded for the RHEM discharge and sediment calibrations at Price.

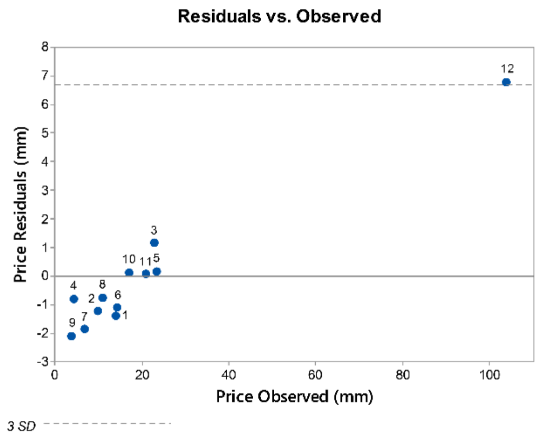

Figure 8: Residuals versus observed for the Price RHEM discharge calibration that included plot 12.

4.3.5 RHEM Model Performance

Performance of the calibrated RHEM model was evaluated using residual plots, the coefficient of determination (R^2), Nash-Sutcliffe efficiency (NSE) [Nash and Sutcliffe, 1970], percent bias (%Bias) [Gupta et al., 1999], ratio of root-mean-squared error to standard deviation (RSR) [Legates and McCabe, 1999], RHEM output residual range proportion to the observed range of sediment or discharge (PRO), and the root-mean squared error to observed range of sediment or discharge values (RMSE/ORA). Residuals were calculated by:

$$Residuals = \sum_{i=1}^{n}(P_i - O_i) \qquad (16)$$

Range of the observed values was calculated by:

$$O_{RA} = O_{max} - O_{min} \qquad (17)$$

NSE was calculated by:

$$NSE = 1 - \frac{\sum_{i=1}^{n}(O_i - P_i)^2}{\sum_{i=1}^{n}\left(O_i - O_{avg}\right)^2} \qquad (18)$$

%Bias was calculated by:

$$\%Bias = \frac{\sum_{i=1}^{n}(O_i - P_i) * 100}{\sum_{i=1}^{n}(O_i)} \qquad (19)$$

RSR was calculated by:

$$RSR = \frac{\sqrt{\sum_{i=1}^{n}(O_i - P_i)^2}}{\sqrt{\sum_{i=1}^{n}(O_i - O_{avg})^2}} \qquad (20)$$

Standard deviation (SD) was calculated by:

$$SD = \sqrt{\frac{1}{n}\sum_{i=1}^{n}(X_i - \mu)^2} \qquad (21)$$

Proportion was calculated by:

$$PRO = \frac{4SD(Residuals)}{O_{RA}} \qquad (22)$$

RMSE/ORA was calculated by:

$$\frac{RMSE}{O_{RA}} = \frac{\sqrt{\frac{\sum_{i=1}^{n}(O_i - P_i)^{\,2}}{n}}}{O_{max} - O_{min}} \qquad (23)$$

Where n is the number of the plot, P_i is the simulated value by the model for the corresponding ith plot, O_i is the observed ith plot to be evaluated, $Omax$ is the maximum observed value, $Omin$ is the minimum observed value, O_{avg} is the average of the observed plot values, X_i is the ith value to be evaluated, and μ is the population mean.

4.3.6 RHEM Sensitivity Analysis

Sensitivity analysis was done to determine: (1) how varying the Kss, $K\omega$, and Ke input parameters affect the discharge and sediment outputs of the RHEM model and (2) how varying VCC affects the discharge and sediment outputs of the model. The model was run with Kss, $K\omega$, and Ke input parameters that were modified from calibrated values for each plot by -50% to 50% in 10% increments to measure the sensitivity of these three parameters on the discharge and sediment outputs across all plots. The model was also run for each plot using calibrated parameters, but substituting a range of VCC from 0% - 100% in 10% increments and graphing changes in discharge and sediment outputs across all plots. For VCC runs, plant basal area and litter were changed in proportion to their observed presence. Note that with high shrub foliar cover, 100% VCC relates to the projected canopy over the plot area, not continuous ground cover like turf.

4.3.7 Vegetation Spatial Distribution Analysis

The spatial distribution of VCC and its influence on the residuals of the sediment output was analyzed using landscape pattern descriptions by McGarigal and Marks [1995]. All the available class level (class 1 = soil, class 2 = vegetation) and landscape level pattern metrics (area-edge, shape, core area, contrast, and aggregation) were calculated using Fragstats v4.2. Edge depth (i.e. edge effect) and search radius of aggregation metrics were set to 1 m, and the threshold distance for CONNECT (aggregation metric that describes how connected the patches are) was set to 0.1 m. Edge contrast and similarity tables were set up so the soil class edge effect penetrates 1 m into the vegetation class. Edge depth, edge contrast, and similarity were set to these values since the plot itself is only 2 m wide. The threshold distance for CONNECT was set to this small value because it was assumed any vegetation or soil patch that is within that distance to a neighboring patch would be considered connected. The R^2 was calculated between all the metrics and the RHEM sediment output residuals for each plot. Results were analyzed separately for each field site and for both sites combined. Histograms were created (Appendix C; Figures 43 – 45) to assess the distribution of R^2s for all metrics in order to identify whether particular types of metrics were related to unexplained variance in RHEM model sediment outputs. Multiple R^2 values were tested for each metric based on linear regression, quadratic regression, or a linearized form of the variable. Furthermore, we wanted to know if there is a universal landscape or class metric type that could be used for both sites, or if a site-specific selection of pattern metric could be justified.

4.3.8 Sediment as a Proxy for Salinity

RHEM-simulated discharge (mm) and sediment (kg) outputs are representative of the amount of depth in rainfall and sediment that comes off the 12 m^2 plot as runoff and were converted into L and kg/L, respectively. The RMA linear regression model for predicting salinity from sediment (from section *4.3.3*) was used with RHEM-simulated plot-averaged sediment concentrations (kg/L) to predict associated TDS concentrations. The result of this analysis was assessed using RMA linear regression of observed salinity versus predicted salinity, testing the significance of the RMA slope term against the slope of the 1:1 line, determine if the 1:1 line falls within the 95% confidence interval, the root mean squared error (RMSE; equation 5), and the ratio of the root mean squared error to observed range (RMSE/ORA; equation 23). To test the significance of the slope term of the RMA regression against the slope term of the 1:1 line, the following equation was used:

$$SIG = \frac{b_{1:1} - b_1}{SE\ Coefficient} \qquad (24)$$

where $b_{1:1}$ is the slope term of the 1:1 line and b_1 is the slope term of the regression. If SIG ≤ 1, this indicates the regression is unbiased. If SIG > 1, the slope term of the regression is significantly different than the slope term of the 1:1 line indicating the regression is biased and our method should be re-evaluated.

5 Results

5.1 *Differences between the Tununk and Blue Gate*

Principal component analysis (PCA) of runoff water at the Price and Dry-X field sites showed that the first principal component (PC1) explains almost half the variation (45%) in measurements and PC2 explains an additional 20% (Figure 9). PCA results for soil chemistry (control and post-rainfall samples; Figure 10) show that the PC1 explains a third of the variation (34%) in measurements and the PC2 explains an additional 20%. In each case, there is limited overlap between the two sites evident by PC1. Table 3 shows the first and second principal component coefficients for each ion for runoff and soil chemistry. For PC1 of runoff, Na^+ and K^+ show the greatest contrast against SO_4^2 and Cl^-. For PC1 of soil, Na^+ and NH_4 show the greatest contrast against Ca^{2+} and Mg^{2+}.

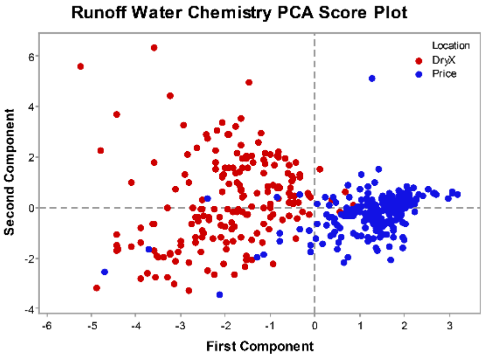

Figure 9: PCA score plot of runoff water chemistry.

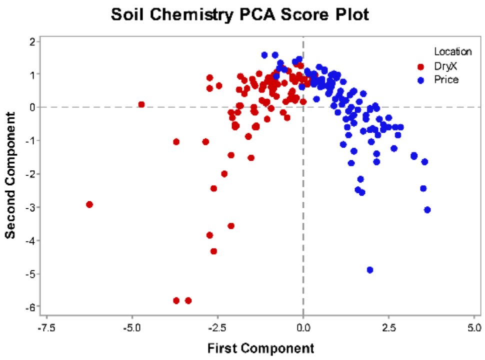

Figure 10: PCA score plot of soil chemistry.

Table 3: First principal coefficients for each ion for runoff and soil chemistry PCA.

Runoff Principal Component (PC) Coefficents

PC	Ca^{2+} meq/L	Mg^{2+} meq/L	Na^{+} meq/L	K^{+} meq/L	NH_4^{+} meq/L	NO_3^{-} meq/L	SO_4^{2-} meq/L	Cl^{-} meq/L
1	-0.351	0.108	-0.464	-0.447	-0.199	0.283	0.408	0.406
2	-0.464	-0.482	0.134	0.069	0.594	0.028	0.388	-0.163

Soil Principal Component (PC) Coefficents

PC	Ca^{2+} meq/L	Mg^{2+} meq/L	Na^{+} meq/L	K^{+} meq/L	NH_4^{+} meq/L	NO_3^{-} meq/L	SO_4^{2-} meq/L	Cl^{-} meq/L
1	0.489	0.415	-0.272	0.393	-0.268	0.083	0.377	0.373
2	-0.043	-0.26	-0.161	-0.478	0.094	0.624	0.154	0.504

Box-and-whisker plots show that runoff salinity (Figure 11), runoff sediment (Figure 12), soil SAR (Figure 13), and soil CEC (Figure 14) are substantially different between the two field sites.

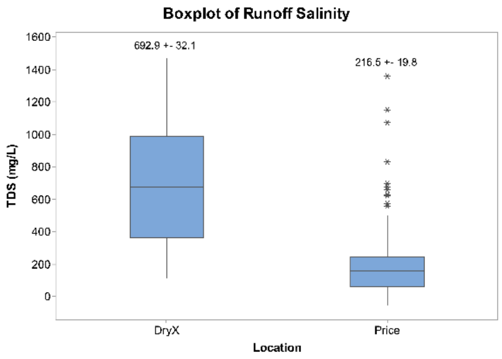

Figure 11: Boxplot of runoff TDS (mg/L).

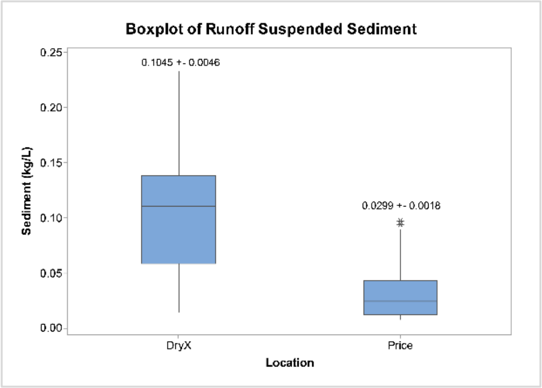

Figure 12: Boxplot of runoff sediment (kg/L).

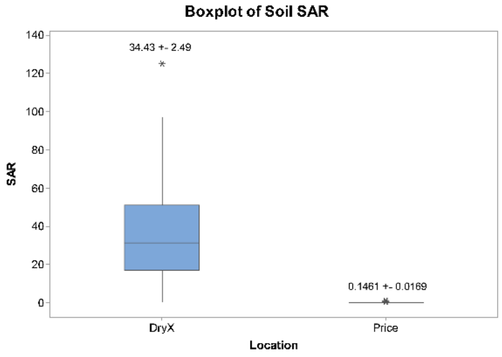

Figure 13: Boxplot of soil SAR.

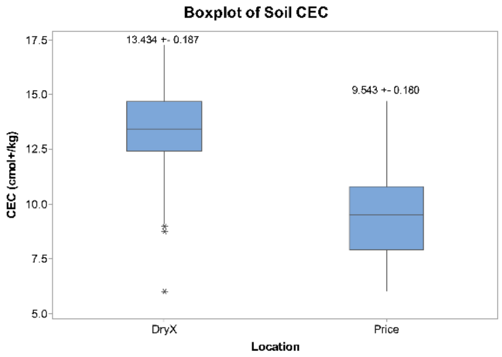

Figure 14: Boxplot of soil CEC (cmol+/kg).

5.2 Relationship between Sediment and TDS

RMA linear regression was used to determine the relationship and significance between sediment concentration (kg/L) and TDS concentration (mg/L) of runoff in erosion processes and whether predicted sediment concentration from RHEM could be used as a proxy to estimate TDS concentration. Using the plot averages, a strong, positive relationship exists between sediment concentration and TDS concentration (Figure 15). Average sediment concentration significantly predicted average TDS concentration ($p < 0.001$, $R^2 = 0.819$) and the RMA linear model did not over-fit the data ($R^2_{pred} = 0.775$).

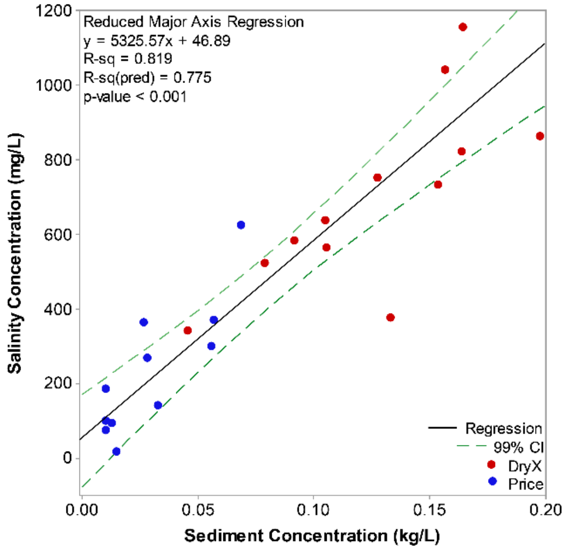

Figure 15: Regression of plot-averaged sediment concentration versus plot-averaged TDS concentration.

5.3 RHEM Calibration

RHEM input parameters were calibrated to match field-measured values of discharge and sediment. Figures 16 and 17 display Pareto plots of optimal calibrated solutions with the selected solution indicated as a black circle. Table 4 shows the range of values used in the calibration to find a set optimized of solutions with low |%Bias| and RMSE for both discharge and sediment.

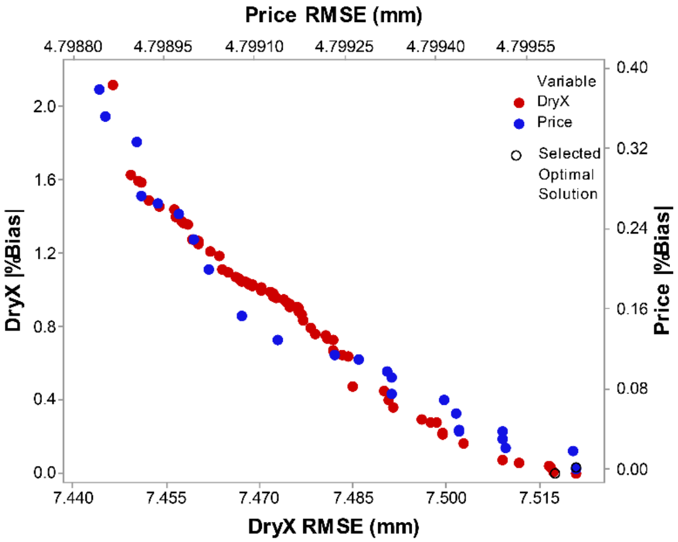

Figure 16: Pareto plot of calibrated RHEM solutions for discharge at Price and Dry-X.

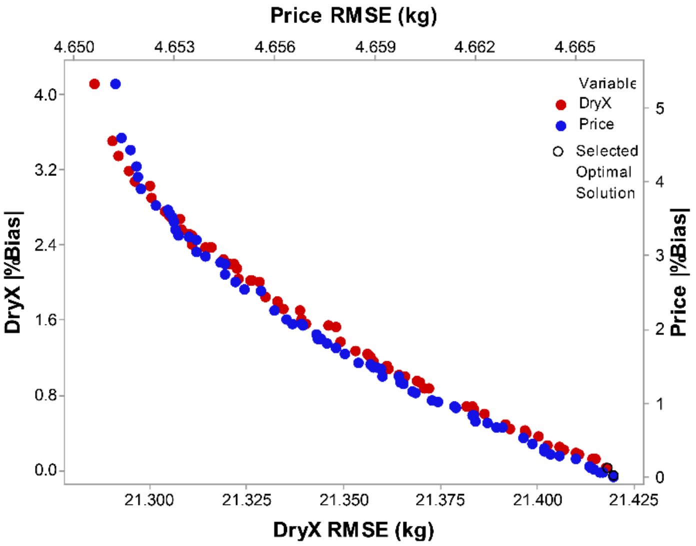

Figure 17: Pareto plot of calibrated RHEM solutions for sediment at Price and Dry-X.

Table 4: Calibration ranges and results for parameters controlling discharge and sediment at both sites.

Calibration	Site	Variable	Calibration Range	Calibrated Value	|%Bias|	RMSE
Discharge	Price	SAT	0.02 - 0.08	0.066	0.0002	4.8 mm
		Ce	0.1 - 10	0.349		
		ALF	0.25 - 1	0.952		
	Dry-X	SAT	0.02 - 0.08	0.064	0.01	7.52 mm
		Ce	0.1 - 10	5.575		
		ALF	0.25 - 1	0.279		
Sediment	Price	Css	0.1 - 10	1.751	0.01	4.67 kg
		Cω	0.1 - 10	3.755		
	Dry-X	Css	0.1 - 10	3.11	0.025	21.42 kg
		Cω	0.1 - 10	3.287		

For discharge, Price had an optimized solution set with a |%Bias| of 0.0002% and a RMSE of 4.8 mm and Dry-X had a higher |%Bias| of 0.01% and RMSE of 7.3 mm. Both sites had similar SATs, but Price had an ALF of 0.952 which is substantially higher than the ALF for Dry-X of 0.279. For sediment, Price had an optimized solution set with a |%Bias| of 0.01% and a RMSE of 4.7 kg whereas Dry-X had a higher|%Bias| of 0.025% and a substantially higher RMSE of 21.1 kg. The calibrated site Ce and Css for the Price site is substantially lower than Dry-X, but $C\omega$ was higher at Price than at Dry-X.

5.4 RHEM Model Performance

Table 5 shows the results of the calibrated RHEM performance. At both field sites the R^2 and NSE was higher for discharge than for sediment. For both discharge and sediment, Dry-X had a higher R^2 and NSE than Price. In all cases except for Dry-X sediment, the residual bias was negative so the calibrated model underestimated slightly. The RSR was lower for discharge than for sediment and Dry-X had lower RSR values than Price. PRO for discharge and sediment was higher for Price than Dry-X. Even though Dry-X had higher RMSE for both calibrations, the lower RMSE/ORA values at Dry-X indicate relatively better calibrations than Price. Overall, calibrated RHEM modeled field conditions at Dry-X better than Price.

Table 5: Model performance results.

Model Performance

Location	Sediment/Discharge	R^2	NSE	%Bias	RSR	PRO	RMSE/ORA
Price	Discharge	0.764	0.745	-0.0002	0.414	0.705	0.176
Dry-X	Discharge	0.799	0.779	-0.01	0.417	0.579	0.145
Price	Sediment	0.444	0.439	-0.01	0.709	1	0.25
Dry-X	Sediment	0.641	0.627	0.025	0.543	0.809	0.202

Figures 18a-b and 19a-b show the residuals for RHEM outputs of the sediment and discharge. The residual ranges for both sediment and discharge at Price are substantially lower than Dry-X. In addition, Price sediment and discharge residuals (Figures 18a-b) show that the RHEM model fits the overall site average, but doesn't capture the plot-

plot variability and a trend exists showing the model over-predicts with low observed values and under-predicts with high observed values. At Dry-X, the RHEM model captured the site and plot-to-plot variability well (Figure 19a-b). For both sites, no outliers exist and all data fall within three standard deviations.

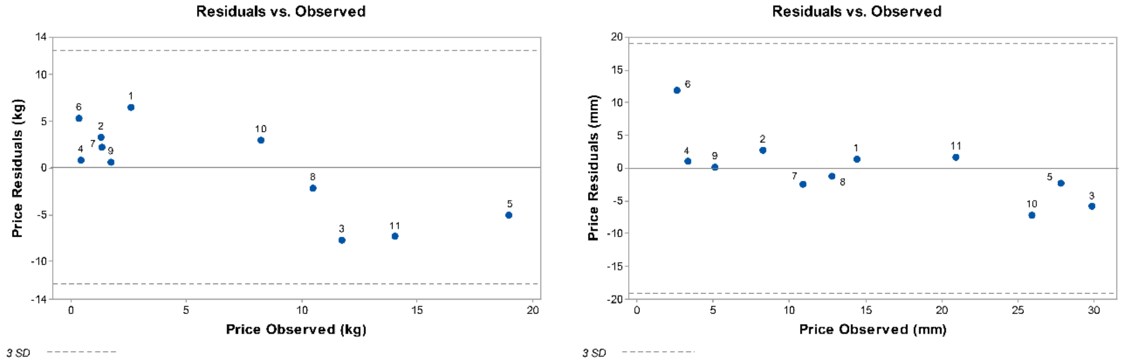

Figure 18a-b: Residual plots of RHEM model outputs for sediment and discharge at Price.

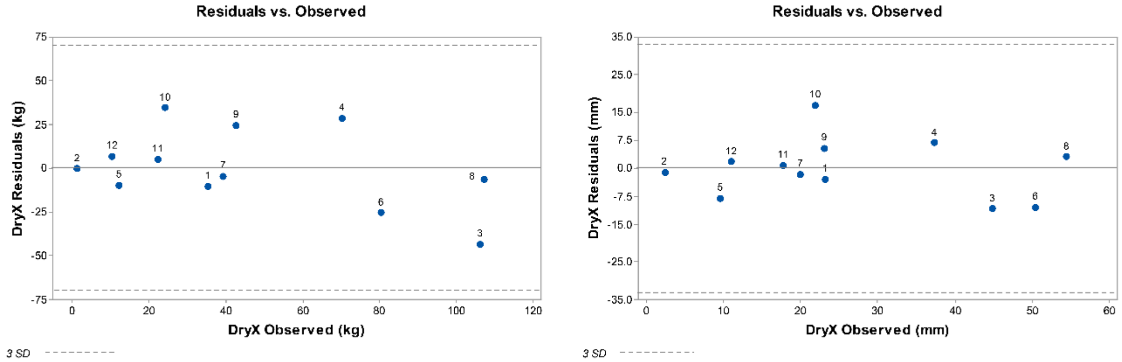

Figure 19a-b: Residual plots of RHEM model outputs for sediment and discharge at Dry-X.

5.5 *RHEM Sensitivity Analysis*

The sensitivity analysis of how changes in Kss, $K\omega$, and Ke and changes in amount of VCC impact discharge and sediment predictions is shown in Figures 20 through 22. Figure 20 shows that Kss has the greatest impact on sediment (84.1% change) and Figure 21 shows that Ke has the greatest impact on discharge (32.9% change). Figure 22 shows that as expected, increasing VCC results in less sediment and discharge. If no vegetation is present, RHEM predicts a 111% increase in sediment and a 4% increase in discharge. With ~8% and ~18% VCC at Price and Dry-X, there is no change to the discharge and sediment outputs since these values represent a non-linear weighting of actual plot values. Lastly, at 100% VCC, RHEM predicts a 91% reduction in sediment and a 55% reduction in discharge.

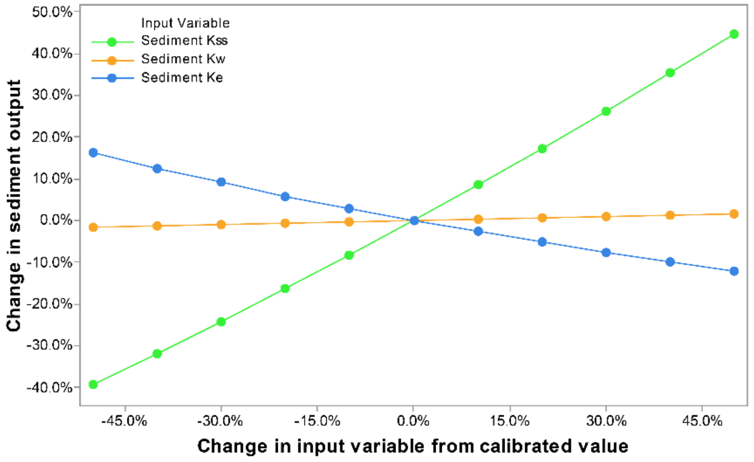

Sed Kss range = 84.1% *Sed Kw range = 3%* *Sed Ke range = 28.4%*

Figure 20: Sensitivity of change in Kss, $K\omega$, and Ke on sediment output.

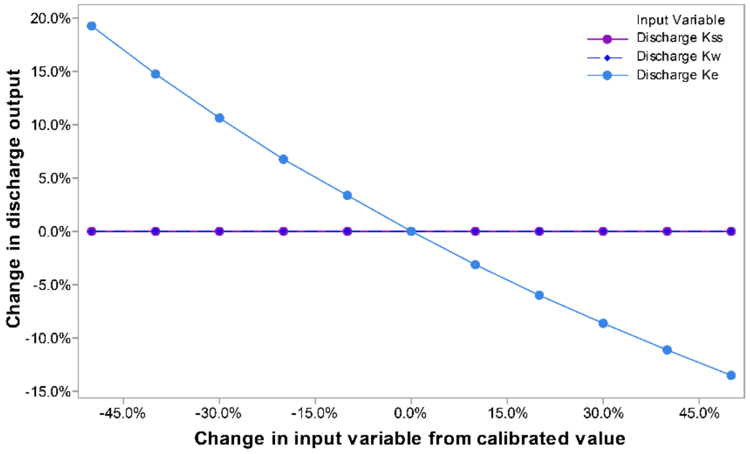

Q Kss & Kw range = 0%

Q Ke range = 32.9%

Figure 21: Sensitivity of change in Kss, $K\omega$, and Ke on discharge output.

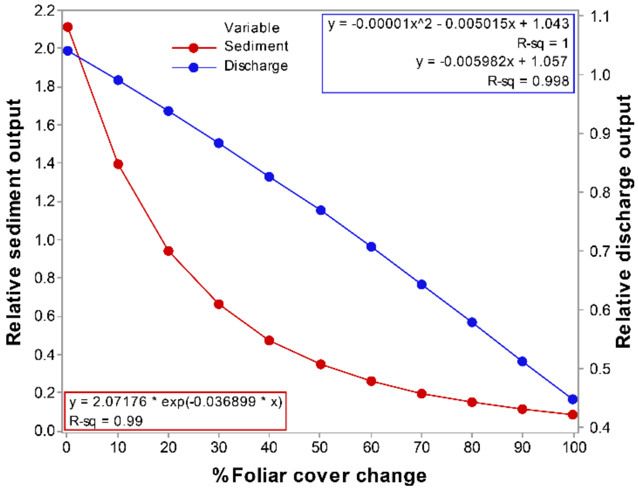

Figure 22: Sensitivity of change in foliar cover on sediment and discharge outputs.

5.6 Vegetation Spatial Distribution Analysis

The spatial distribution of vegetation was analyzed using metrics of landscape pattern. Landscape level and class level (soil and vegetation) metrics were analyzed for both sites individually and together, using regression against the calibrated RHEM sediment residuals to assess if the spatial distribution of VCC may have an effect on sediment erosion. The results are summarized in Table 6.

Table 6: R^2s for linear regressions of selected spatial pattern metrics versus RHEM sediment output residuals.

Metric	Location	R^2	Slope	p-value	Name	Type
Landscape	Both	0.27	-	0.012	ENN_AM	Aggregation
	Price	0.33	-	0.065	ENN_RA	Aggregation
	Dry-X	0.38	-	0.034	ENN_AM	Aggregation
Class - Soil	Both	0.46	+	<0.001	FRAC_CV	Shape
	Price	0.21	-	0.155	CIRCLE_MN	Shape
	Dry-X	0.59	+	0.004	FRAC_CV	Shape
Class - Veg	Both	0.43	-	0.001	GYRATE_MD	Area-Edge
	Price	0.35	+	0.054	ECON_RA	Contrast
	Dry-X	0.60	+	0.003	PROX_MD	Aggregation

The selection of landscape metrics for relating vegetation canopy and soil interspace pattern to model residuals of sediment shared the same aggregation metric. Euclidean nearest neighbor distance (ENN) is an aggregation metric that is a simple measure of patch isolation [McGarigal, 2015] and was always inversely proportional to RHEM sediment residuals. With both sites combined, the selection of ENN_AM (Figure 23a) is significant; however, the residuals do not have a normal distribution. The best selection of ENN_RA for Price (Figure 24a) is not statistically significant. The selection of ENN_AM for Dry-X has the highest R^2 (Figure 25a) among landscape level metrics and is significant. However, the regression is mainly driven by one point and if that point is omitted, R^2 reduces to nearly zero and is no longer significant.

The selection of class metrics for relating soil pattern to model residuals of sediment were all shape metrics. Fractal dimension index (FRAC) is a shape type metric that describes the shape complexity of the object [McGarigal, 2015]. Selected class metrics for the pattern of soil interspaces at both sites were all shape metrics and all except for Price were proportional to RHEM sediment residuals. With both sites combined, the selection of FRAC_CV (Figure 23b) is significant; however, the residuals do not have a normal distribution. The best selection for Price, CIRCLE_MN (Figure 24b), is not statistically significant. CIRCLE is a shape metric that describes the ratio of patch area to the area of the smallest circumscribing circle (patch elongation) [McGarigal, 2015]. As the soil patch elongation decreases, the model over-predicts sediment. The selection of FRAC_CV for Dry-X had the highest R^2 (Figure 25b) among the class level metrics for soil and is significant. As the shape complexity of soil interspaces increases, the model over-predicts sediment.

The selection of class metrics for relating vegetation canopy pattern to model residuals of sediment did not share a common type of metric like the landscape and soil class metrics did, and except with both sites combined, all selected metrics were proportional to the RHEM sediment residuals. With both sites combined, the regression between residuals and = radius of gyration (GYRATE_MD; Figure 23c) is significant. However, the regression is partially driven by one point and if that point is omitted, R^2 is reduced by half but still remains significant. GYRATE is an area-edge type metric that measures of the maximum patch extent. As the VCC patch extent decreases, the model over-predicts sediment. The best selection for Price, the edge contrast index (ECON_RA; Figure 24c), is not significant. ECON measures the degree of contrast between the patch and its immediate neighborhood [McGarigal, 2015]. As the contrast between the VCC patch and its immediate neighborhood increases, the model over-predicts sediment. The best selection for Dry-X, the proximity index (PROX_MD; Figure 25c) has the highest R^2 among the class level metrics for vegetation and is significant, but the residuals do not have a normal distribution. PROX is an aggregation type metric that measures both the degree of patch isolation and fragmentation of the corresponding patch type within the specified neighborhood of the focal patch [McGarigal, 2015]. As the degree of patch isolation and fragmentation of VCC increases, the model over-predicts sediment. Using quadratic regression in an attempt to improve R^2, both sites combined and Dry-X landscape and class level metrics showed improvement in R^2 (Figures 26a-f). Quadratic regressions were done for Price in the same way in an attempt to improve R^2 and the p-value, but none of them showed improvement. However, all the residuals except for landscape and soil class level for Dry-X did not have a normal distribution. All original Dry-X regressions were linearized, but only PROX resulted in a substantial improvement in R^2. PROX was linearized by $1/\text{Log}_{10}(\text{PROX})$ and the residuals have a normal distribution (Figure 27).

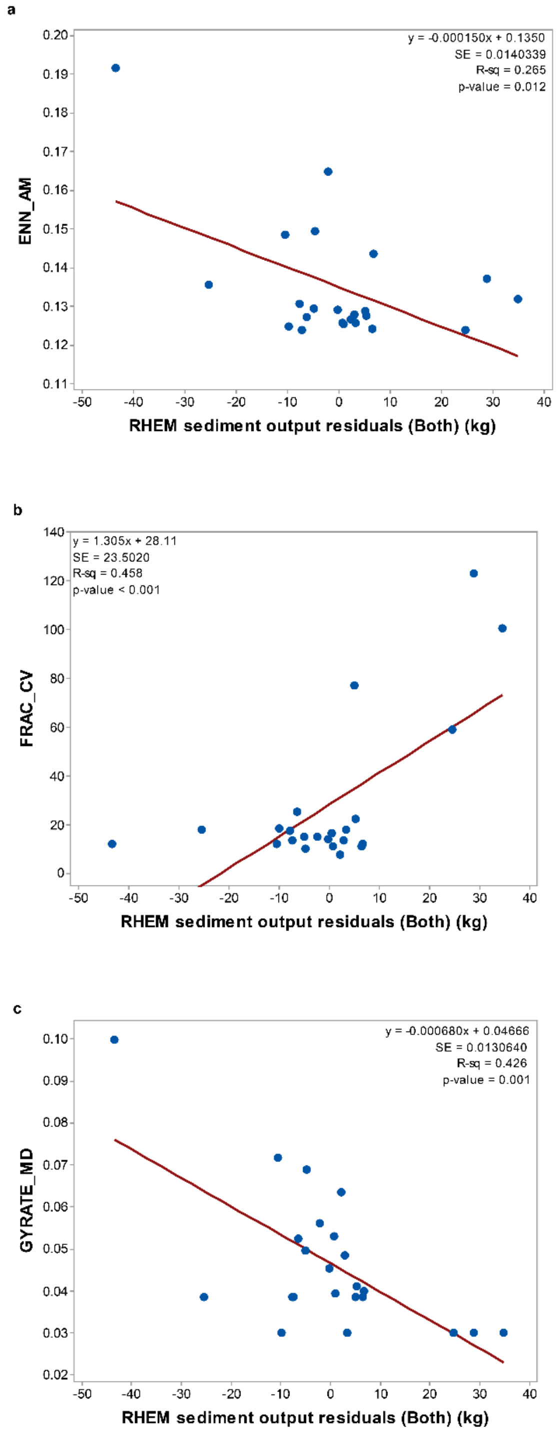

Figure 23a-c: Linear regressions of (a) landscape metric, (b) soil class metric, and (c) vegetation class metric versus RHEM sediment output residuals for both sites.

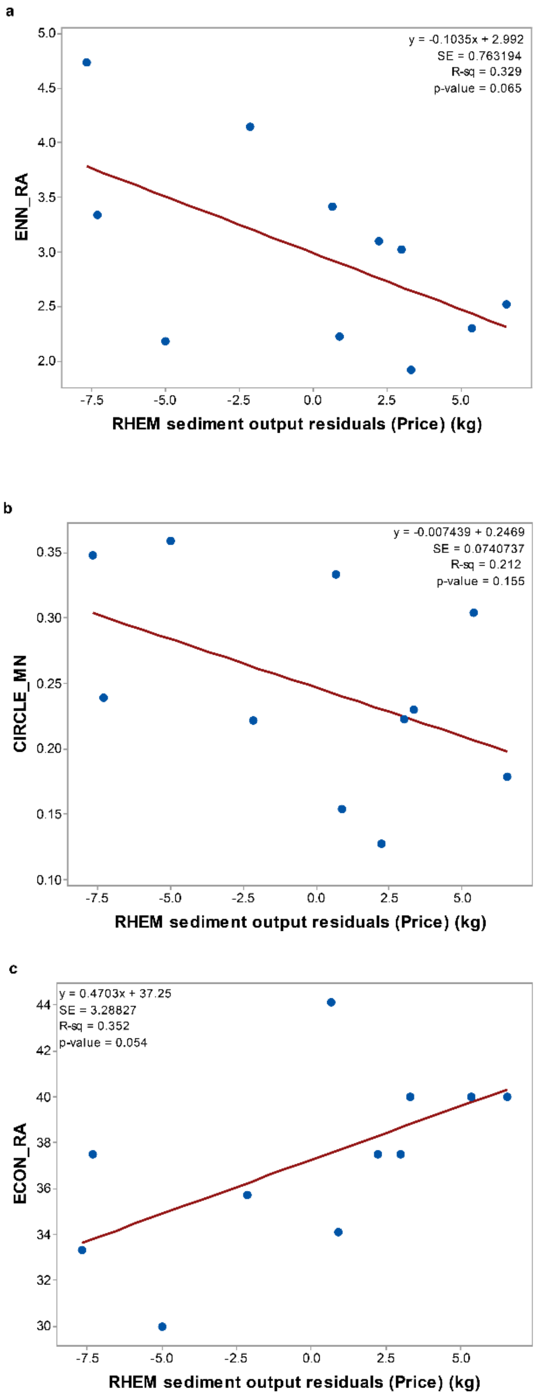

Figure 24a-c: Linear regressions of (a) landscape metric, (b) soil class metric, and (c) vegetation class metric versus RHEM sediment output residuals for Price.

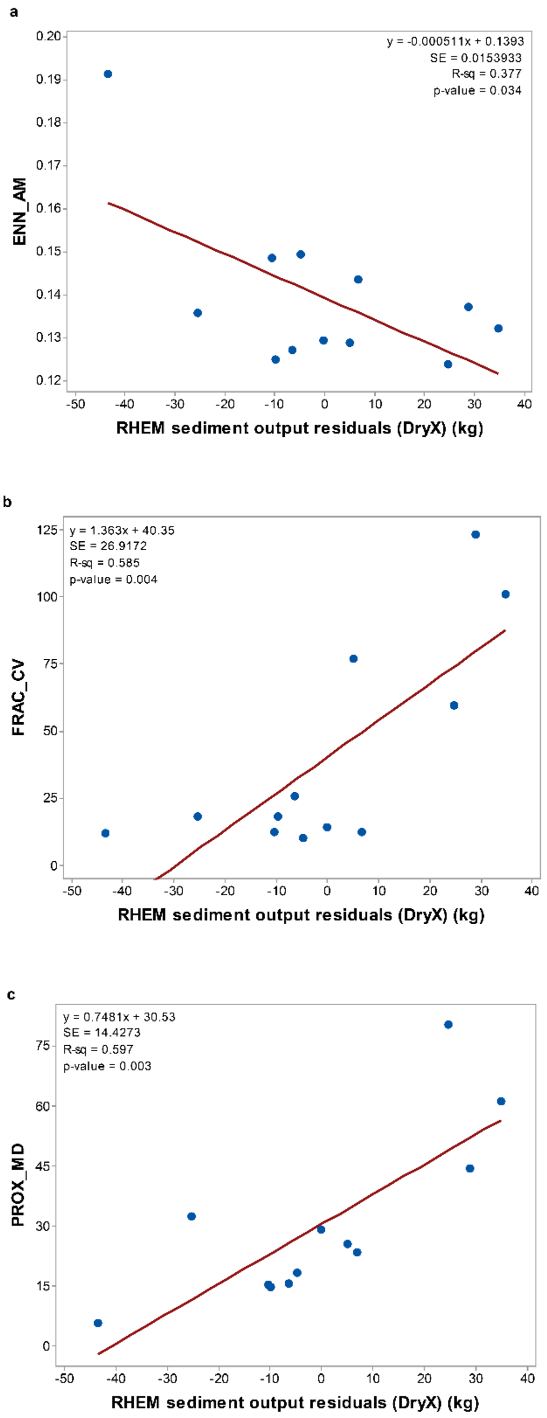

Figure 25a-c: Linear regressions of landscape metric, soil class metric, and vegetation class metric versus RHEM sediment output residuals for Dry-X.

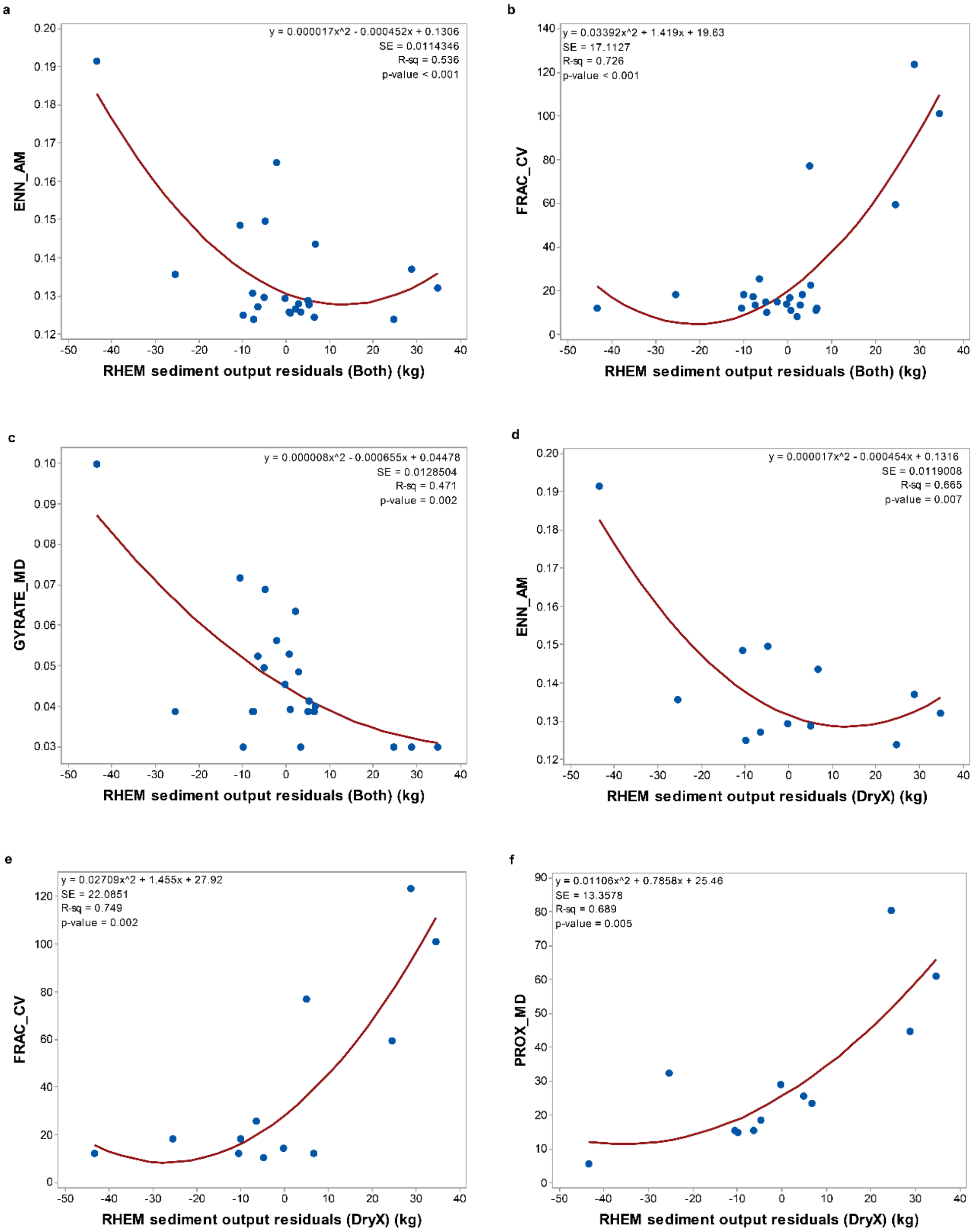

Figure 26a-f: Quadratic regressions of landscape metric, soil class metric, and vegetation class metric versus RHEM sediment output residuals. (a-c) Quadratic regressions of landscape metric, soil class metric, and vegetation class metric versus RHEM sediment output residuals for both sites. (e-f) Quadratic regressions of landscape metric, soil class metric, and vegetation class metric versus RHEM sediment output residuals for Dry-X.

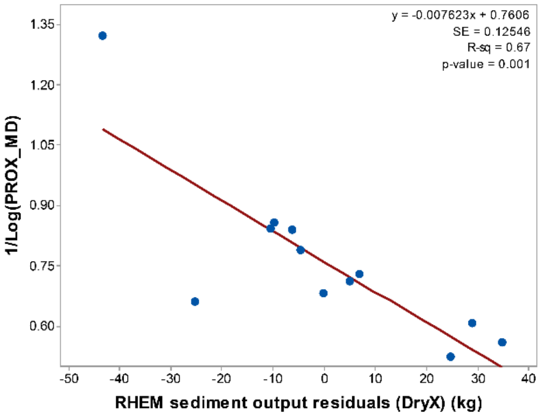

Figure 27: Linearized regression of PROX_MD versus RHEM sediment output residuals for Dry-X.

Overall, with the presence of greater VCC at Dry-X, certain landscape metrics indicate a possible relationship between the pattern of VCC, soil interspaces, and the RHEM sediment output residuals.

5.7 Sediment as a Proxy for Salinity

Applying the plot-averaged simulated sediment data from RHEM to the RMA linear regression model (section *4.33*; Figure 15) showed a strong, positive linear relationship exists between observed and predicted TDS concentration (Figure 28). Observed TDS concentration significantly predicted TDS concentration ($p < 0.001$, $R^2 = 0.73$) and the linear model did not over-fit the data ($R^2_{pred} = 0.673$). The regression line has a similar trend as the 1:1 line with a slight positive bias driven by the Price data. The slope term of the RMA linear regression was found to not be significantly different from the slope term of the 1:1 line ($SIG < 1$) and the 1:1 line falls within the 95% confidence interval (CI). The RMSE between observed and predicted TDS concentration is 170.2 mg/L and the ratio of RMSE to O_{RA} is 0.149 indicating that the linear regression model provides valid predictions with a low error relative to the observed range.

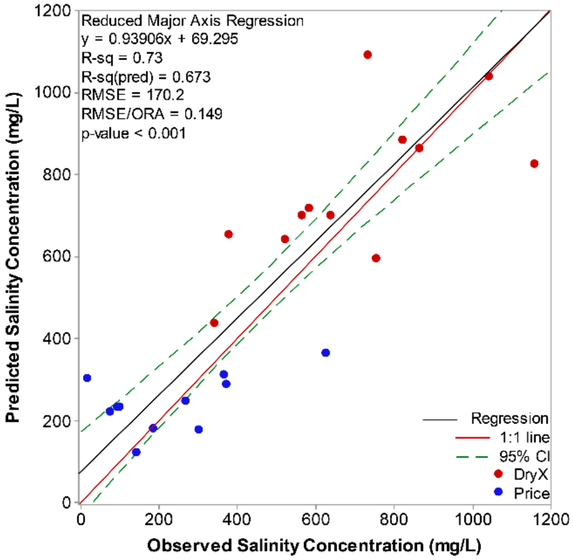

Figure 28: Regression of the observed TDS concentration versus the predicted TDS concentration relative to the 1:1 line.

6 Discussion

The Price and Dry-X field sites are located on the Mancos Shale formation and were assumed to be comparable during the reconnaissance trip. When field work began, the differences between the sites were more apparent in terms of the amount and spatial distribution of VCC, slope, soil color and development of soil crusts, and presence of salt efflorescence (Figure 5a-b). Site selection was coordinated with the BLM and was strongly influenced by accessibility constraints which led to sites being selected on the Mancos Shale formation regardless of the geologic member (Figure 3a-b). The PCA results for runoff water chemistry (Figure 9; Table 3) show the sites produce different runoff chemistries. When looking at the runoff ion concentration means for both sites, we see that all four ion concentrations at Dry-X are substantially higher than at Price and the PCA results for soil chemistry (Figure 10; Table 3) show that the sites have different soil chemistries. When looking at the soil ion means for both sites, we see that Na^+ and NH_4^+ concentrations at Dry-X are substantially higher than at Price and the ratio of Ca^{2+} to Mg^{2+} is higher at Dry-X than at Price, even though Price has higher Ca^{2+} and Mg^{2+} concentrations. PC2 for both sets of results didn’t show any added value to explain the differences in variability among the ions between sites. Dry-X produced substantially more TDS and sediment in runoff (Figures 11-12), the soils are more saline and sodic than Price (Figure 13), and had higher average soil CEC (Figure 14). These results collectively suggest the difference in geologic members and their respective depositional environments during the late Cretaceous may reflect differences in parent material that drives the differences in soil development in arid climates. The differences in soil characteristics may result in the noticeable differences in runoff water and soil chemistry between sites.

There is little literature on the relationship between sediment erosion and salinity transport processes. Variable factors have been proposed to explain the complex relationship. Laronne and Shen [1982] suggest that precipitation and initial runoff being under-saturated with respect to soil minerals, slope at the site, runoff rate, rill development, and dissolution of sediment particles may contribute to the relationship. In addition, Evangelou [1981] showed that the release of ions from the Mancos Shale is directly related and regulated by the soil exchange complex and the relative cation adsorption affinities of the soil minerals. Our findings (Figure 15) suggest that a significant and strong relationship exists between plot-averaged sediment and salinity in runoff, and the regression model provides valid predictions. Furthermore, Ponce [1975] found significant correlations between salinity and sediment production on individual plots from different geologic members, but by taking the plot-average, we have shown a strong linear relationship between sediment and salinity erosion processes across both sites. This result suggests more erosive geologic members of the Mancos Shale may produce higher values of sediment and salinity than less erosive geologic members and may indicate a linear relationship at the geologic formation level.

The RHEM calibration results for both Price and Dry-X discharge and sediment (Figures 16 - 17) had solutions with low RMSE and |%Bias|. Currently, the RHEM model uses three parameters that relate the amount of vegetation to erosion processes: Kss, Kw, and Ke. Our results (Table 4) show that for saline and sodic soils of the Mancos Shale, the calibrated values for all three input parameters were higher than originally estimated from the model documentation and associated equations(e.g. RHEM [2015], Al-Hamdan et al. [2015]; equations 9 - 12). In addition, RHEM hasn't been calibrated for undisturbed saline and sodic soil before indicating new parameter equations may be required. Furthermore, Ke and Kss at Dry-X were substantially greater than Price, but Kw was lower at Dry-X. The model performed well for both discharge and sediment at both field sites (Figures 18 – 19a-b). However, at Price, the model for both sediment and discharge (Figures 18a-b) overestimated low observed values and underestimated high observed values, indicating RHEM doesn't capture the plot-plot variability as well at Price compared to Dry-X. These results also are reflected in Table 5 where Price had a lower R^2 and NSE as well as a higher RSR, PRO, and RMSE/ORA for both discharge and sediment, indicating the model performed better simulating Dry-X conditions than Price. The disparity between how RHEM is handling the plot-plot variability at Price and Dry-X may be related to the low VCC, slope, soil SAR, and even the soil crusts found at Price. Other studies were more successful at capturing plot level variability because RHEM has been calibrated for non-saline and sodic rangelands soils with variable VCC and slope on burned, disturbed, and undisturbed plots in the past (Al-Hamdan et al. [2015; 2012]; Nearing et al. [2011]; Felegari et al. [2014]). Overall, this study showed that RHEM can be calibrated to simulate sediment erosion and hydrologic processes on rangeland saline and sodic soils of the Mancos Shale formation and calibrated Kss, $K\omega$, and Ke are higher than calibrated values from previous studies done on non-saline and sodic soils.

VCC intercepts raindrop impact and reduces runoff volumes [Wischmeier and Smith, 1978] and promotes increased infiltration with increasing VCC [Loch, 2000] by stemflow [Branson et al., 1972]. The sensitivity of the calibrated RHEM sediment and discharge outputs to Kss, Kw, and Ke parameters and to foliar cover show that RHEM has a capacity to simulate these processes. The equations for these parameters allow VCC to reduce in splash and sheet erosion, concentrated flow erosion (Figure 20), and increase infiltration (Figure 21) in RHEM. Of these three parameters, Kss is the most sensitive, indicating that VCC reduces predicted sediment loading mostly by reducing splash and sheet erosion. In addition, we found that as foliar cover increases, sediment and discharge decreases (Figure 22) in RHEM.

Bartley et al. [2006] conducted a hillslope-scale study on savanna rangelands in Australia and found that even with high mean VCC, small patches of interspace had substantially more runoff and sediment than similar hillslopes with less or no interspace patches. In addition, the sediment load consisted of fine suspended sediment and the majority of soil loss occurred during the initial runoff event. Observed sediment loss (fine suspended sediment) at plots 1, 2, 4, and 5 at Price and plots 4, 6, and 5 at Dry-X was higher during the initial runoff event. On almost all plots at Price (except 1, 11, and 12), observed salinity loads were higher during the initial runoff event. It is likely plots 11 and 12 didn't show the same trend as the others because of the coarse sampling interval used at those plots. Interestingly, our sensitivity results (Figure 22) show that with moderate VCC (50%) to maximum VCC (100%), there is a continuous reduction in simulated sediment and discharge and the difference in magnitude of simulated sediment loss between 50% VCC and 100% VCC is within the same order of magnitude which is not in agreement with the findings of Bartley et al. [2006]. It's not clear if the discrepancy between our sensitivity results and Bartley et al. [2006] is due to the differences in vegetation types or the default value for uniform interception depth that we used to calibrate the model which in reality, may be highly variable especially at Price since it contained more than one plant species.

Puigdefabregas [2005] suggests that VDSH explains the relationship between soil development and evolution processes and in turn, influences sheet and concentrated flow processes [Wilcox et. al, 1996; Davenport et al., 1998; Urgeghe et al., 2010]. Our results indicate that VDSH is significantly correlated with RHEM sediment output residuals from sites with variable VCC (3.3% - 26.4%), slope (0.7% - 24.5%), and rainfall intensity. The results were statistically significant at both sites combined and at Dry-X ($p < 0.05$), but not at Price by itself ($p > 0.05$). The results from both sites combined (Figure 23a-c; Figure 26a-c) show the regressions were mainly driven by Dry-X data because the Price residual and spatial pattern metric range was substantially smaller compared to Dry-X. This suggests that there is not a single metric that will adequately work for both sites given the limited overlap in the VCC variability between sites. In addition, the results from Price (Figure 24a-c) were likely not significant because of the low amount of VCC and slope present and the poor ability of RHEM to capture the plot-plot variation (Figures 18a-b; Table 5) despite fitting the overall site response.

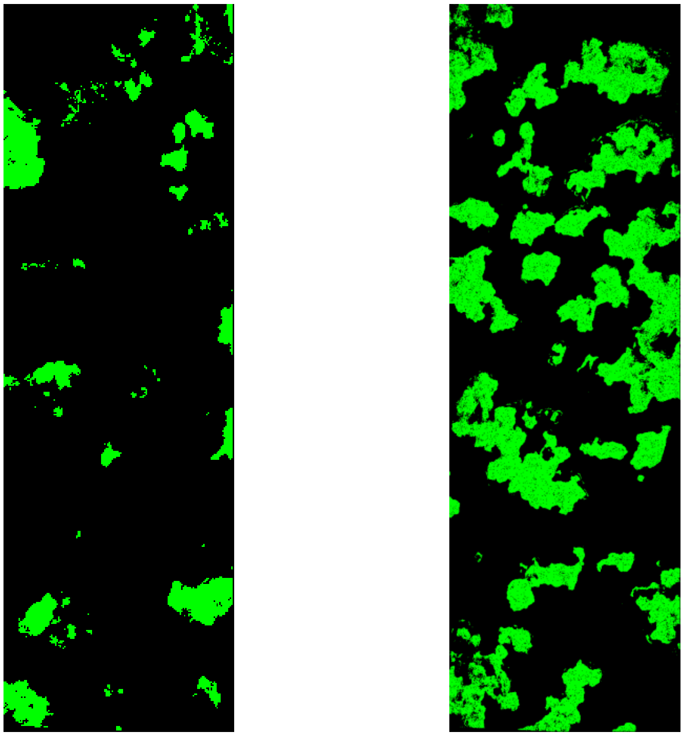

Figure 29a-b: (a) Vegetation map of Price plot 5 and (b) of Dry-X plot 10. Green = vegetation and black = soil.

Price contains a low amount of VCC and the vegetation patches are small, isolated, and have simple shape complexity (Figure 29a). In contrast, Dry-X contains a higher amount of VCC with large patches that are close together, connective, and have complex shapes (Figure 29b). As a result, the spatial distribution of VCC at Dry-X appears to protect soil patches and create tortuous flow paths compared to Price. At Dry-X, using landscape and class aggregation metrics for vegetation, ENN_AM (Figure 25a) and PROX_MD

(Figure 25c, 27), both show that as the vegetation patches become closer together and more uniform, the model over-predicts sediment in runoff. A similar effect was observed when using FRAC_CV (Figure 25b), which indicates an increase in tortuosity of the soil interspace and therefore flow paths, resulted in less actual sediment in runoff than the model predicts. In addition, Figures 25b and 26e show that at Dry-X using FRAC_CV, the largest four points drive the regression indicating a possible threshold response. The regressions of Dry-X VCC and slope versus the RHEM Dry-X sediment output residuals (Figure 30a-b), show that the relationship of residuals to VDSH is not just a spurious correlation to variability in other important model parameters, since both regressions are insignificant and have a weak R^2. This shows the threshold response observed in Figure 25b may be an actual physical process that is not currently handled well by RHEM.

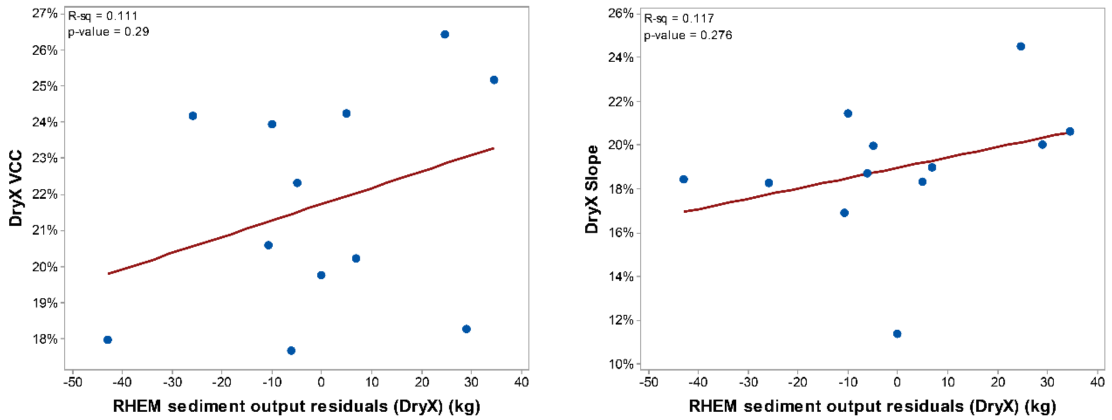

Figure 30a-b: Linear regression analysis of Dry-X (a) VCC and (b) slope versus the RHEM sediment output residuals for Dry-X.

Chartier et al. [2011] proposed VDSH may affect the amount of runoff and infiltration. Interestingly, in the equation of Ke, when the amount of VCC goes up we also see an increase in infiltration, so we would expect Dry-X to have increased infiltration since it has a greater amount of VCC and spatial distribution complexity. Looking at the RHEM discharge calibrations for Price and Dry-X (Table 4), we see that Ce is substantially higher at Dry-X than Price which indicates more infiltration is occurring at Dry-X in the model. These results, and evidence found in the literature cited above, suggest that the spatial distribution of vegetation cover has a significant impact on sediment erosion processes regardless of varying slope, amount of VCC, and rainfall intensity.

Applying RHEM-simulated sediment to the regression model (Figure 15), a strong, significant relationship between the observed TDS and predicted TDS concentration (Figure 28) was found that has relatively low error and the 1:1 line falls with the 95% CI. This indicates that sediment can be used as a proxy to estimate salinity in RHEM using our linear regression model. It also indicates sediment erosion and salinity transport processes are related and by managing soil erosion processes, salinity transport processes will also be affected.

7 Conclusions

In this study, the amount and spatial distribution of VCC had a measurable effect on modelled sediment and salinity loading in runoff over a range of rainfall intensity, slope, VCC, and soil properties using RHEM. RHEM seems to handle the plot-plot variability best at sites with steeper slopes and greater amount of VCC. Landscape pattern descriptions showed that with moderate VCC, as the vegetation patches get closer together, more uniform, and as the soil interspace tortuosity increases, observed sediment loading decreases relative to modeled expectations. In addition, a linear relationship between sediment and TDS concentration was found, and when used to predict TDS concentration using simulated sediment concentration, the relationship predicted TDS concentration from modeled sediment loads. This suggests that a linear relationship between salinity transport and sediment erosion processes can be applied to the RHEM model for the Mancos Shale formation. This study provides new parameterizations for RHEM that will improve its prediction capabilities and value for saline and sodic soils in rangelands of the Mancos Shale formation. The study also provides Upper Colorado River Basin agencies with valuable information that may help reduce sediment and salinity loads into the Colorado River.

The results from this study supported much of the research that has been done, but knowledge gaps still exist. Further research should be done to investigate the following:

1. How sediment and salinity erosion processes during a rainfall event are influenced by the dispersitivity of the soil in relation to the factors presented by Laronne and Shen [1982] and Evangelou [1981] on the various geologic members of the Mancos Shale formation.
2. How VDSH metrics presented in this study may be integrated into RHEM to improve its prediction capabilities.
3. Is there a threshold response associated with soil interspace tortuosity?
4. The role of salt efflorescence (and the specific minerals that make it up) on salinity loading.
5. Why was observed sediment and salinity loading at Price generally higher in the initial runoff event regardless of intensity and why these trends are mostly not observed at Dry-X?

In addition, the experimental design of future research projects may benefit from:

1. Selecting field sites based on geologic members of the selected formation.
2. Collecting soil cores on reconnaissance trips to identify the variability of soil dispersivity between sites.
3. When collecting soil cores, record the infiltration depth and calculate an approximate an average depth for each plot and intensity.
4. Collecting salt efflorescence to begin documenting the evaporate minerals that are present and may be exclusively found on certain geologic members.
5. Collecting soil moisture data (one less parameter to calibrate).

6. Approximating interception depth from collected VCC data.

Lastly, even though these results may provide a possible solution to mitigate the projected increase in sediment and salinity loads into the Colorado River with future climate change, the Upper Colorado River Basin and the agencies that manage it will have to evaluate and create feasible solutions to implement vegetation planting projects that are economical and do not produce adverse side effects such as habitat alterations for local fauna.

8 References

Abrahams A.D., Parsons A.J., Luk S.H. (1991). The effect of spatial variability in overland flow on the downslope pattern of soil loss on a semiarid hillslope, southern Arizona. Catena 18:255-270.

Al-Hamdan, O.Z., Hernandez, M., Pierson, F.B., Nearing, M.A., Williams, C.J., Stone, J.J., Boll, J., Weltz, M.A. (2015). Rangeland hydrology and erosion model (RHEM) enhancements for applications on disturbed rangelands. Hydrological Processes. DOI: 10.1002/hyp.10167.

Al-Hamdan OZ, Pierson FB, Nearing MA, Williams CJ, Stone JJ, Kormos PR, Boll J, Weltz MA. (2013). Risk assessment of erosion from concentrated flow on rangelands using overland flow distribution and shear stress partitioning. Transactions of the American Society of Agricultural and Biological Engineers 56(2): 539–548.

Al-Hamdan O.Z., Pierson F.B., Nearing M.A., Williams C.J., Stone J.J., Kormos P.R., Boll J., Weltz M.A. (2012). Concentrated flow erodibility for physically based erosion models: Temporal variability in disturbed and undisturbed rangelands. Water Resources Research 48. DOI: 10.1029/2011wr011464.

Bartley, R., Roth, C.H., Ludwig, J., McJannet, D., Liedloff, A., Corfield, J., Hawdon, A., and Abbott, B. (2006). Runoff and erosion from Australia's tropical semi-arid rangelands: influence of ground cover for differing space and time scales. Hydrological Processes, 20(15), 3317-3333.

Bauch N.J., Spahr N.E. (1998). Salinity trends in surface waters of the Upper Colorado River Basin, Colorado. Journal of Environmental Quality 27:640-655.

Belnap J., Wilcox B.P., Van Scoyoc M.W., Phillips S.L. (2013). Successional stage of biological soil crusts: an accurate indicator of ecohydrological condition. Ecohydrology 6:474-482. DOI: 10.1002/eco.1281.

Belnap J. (2006). The potential roles of biological soil crusts in dryland hydrologic cycles. Hydrological Processes 20:3159-3178.

Blackburn W., Skau C. (1974). Infiltration rates and sediment production of selected plant communities in Nevada. Journal of Range Management:476-480.

Blackman Jr, W.C., Rouse, J.V., Schillinger, G.R., & Shafer Jr, W.H. (1973). Mineral pollution in the Colorado River basin. Journal (Water Pollution Control Federation), 1517-1557.

Bowles D.S., Nezafati H., Bhasker R.K., Riley J.P., Wagenet R.J. (1982). Salt loading from efflorescence and suspended sediments in the Price River basin, Water Resources Planning Series, Utah Water Research Laboratory, Utah State University, Logan, Utah. pp. 142.

Bower, C.A., Reitemeier, R.F., Fireman, M. (1952). Exchangeable cation analysis of saline and alkali soils. Soil Sci., 73, 251-261.

Branson F.A., Gifford G.F., Owen J.R. (1972). Rangeland hydrology Society for Range Management Denver, Colorado.

Breshears, D.D., Whicker, J.J., Johansen, M.P., & Pinder, J.E. (2003). Wind and water erosion and transport in semi-arid shrubland, grassland and forest ecosystems: Quantifying dominance of horizontal wind-driven transport. Earth Surface Processes and Landforms, 28(11), 1189-1209.

Bundy, L.G., Meisinger, J.J. (1994). Nitrogen availability indices. In: Weaver, R.W., Angle, S., Bottomley, P., Bezdicek, D., Smith, S., Tabatabai, A., Wollum, A. (Eds.), Methods of Soil Analysis. Part 2. Microbiological and Biochemical Properties, Soil Science Society of America, Madison, WI, pp. 951–984.

Carr, J. (2012). Orthogonal regression: A teaching perspective. International Journal of Mathematical Education in Science and Technology, 43(1), 134-10. doi:10.1080/0020739X.2011.573876

Carroll, C., Merton, L., & Burger, P. (2000). Impact of vegetative cover and slope on runoff, erosion, and water quality for field plots on a range of soil and spoil materials on central Queensland coal mines. Soil Research, 38(2), 313-328.

Charley, J. L., & West, N. E. (1975). Plant-induced soil chemical patterns in some shrub-dominated semi-desert ecosystems of Utah. Journal of Ecology, 63(3), 945-963. doi:10.2307/2258613.

Chartier, M.P., Rostagno, C.M., & Pazos, G.E. (2011). Effects of soil degradation on infiltration rates in grazed semiarid rangelands of northeastern Patagonia, Argentina. Journal of Arid Environments, 75(7), 656-661.

Crowe, C.T., Elger, D.F., Williams, B.C., Roberson, J.A. (2009). Engineering Fluid Mechanics, 9th Edition, John Wiley & Sons, Jefferson City.

Davenport D.W., Breshears D.D., Wilcox B.P., Allen C.D. (1998). Viewpoint: Sustainability of pinon-juniper ecosystems: A unifying perspective of soil erosion thresholds. Journal of Range Management 51:231-240.

Domingo F., Puigdefabregas J., Moro M.J., Bellot J. (1994). Role of vegetation cover in the biogeochemical balances of a small afforested catchment in southeastern Spain. Journal of Hydrology 159:275-289.

Eldridge, D.J. (1998). Trampling of microphytic crusts on calcareous soils, and its impact on erosion under rain-impacted flow. Catena, 33(3), 221-239.

Eldridge D.J. (1993). Cryptogam cover and soil surface condition: effects on hydrology on a semiarid woodland soil. Arid Land Research and Management 7:203-217.

Evangelou V.P., Whittig L.D., Tanji K.K. (1984). Dissolved Mineral Salts Derived from Mancos Shale. Journal of Environmental Quality 13:146-150.

Evangelou, V.P. (1981). Chemical and mineralogical composition and behavior of the Mancos Shale as a diffuse source of salts in the Upper Colorado River Basin.

Felegari, M., Talebi, A., Dastorani, M. T., & Rangavar, A. S. (2014). Efficiency Assessment of Rangeland Hydrology and Erosion Model (RHEM) for water erosion quantification (Case Study: Sangane Watershed-Iran). International Journal of Environmental Resources Research, 2(2), 134-146.

Foster GR. (1982). Modeling the erosion process. Chapter 8 in: Hydrologic modeling of small watersheds. In ASAE Monograph No. 5, Haan CT, Johnson HP, Brakensiek DL (eds). American Society of Agricultural Engineers: St. Joseph, MI.; 297–360.

Friedman, J., Bohonak, A. J., & Levine, R. A. (2013). When are two pieces better than one: Fitting and testing OLS and RMA regressions. Environmetrics, 24(5), 306-316. doi:10.1002/env.2213

Geological Survey (US). Orkild, P.P. (1956). Photogeologic Map of the Emery-1 Quadrangle, Emery County, Utah.

Geological Survey (US). Weiss, M.P., Witkind, I.J., Cashion, W.B. (2003). Geologic Map of the Price 30’ x 60’ Quadrangle, Carbon, Duchesne, Uintah, Utah, and Wasatch Counties, Utah.

Geological Survey (US). Witkind, I.J., Weiss, M.P., Brown, T.L. (2006). Geologic Map of the Manti 30’ x 60’ Quadrangle, Carbon, Emery, Juab, Sanpete, and Sevier Counties, Utah.

Geological Survey (US). Witkind, I.J., Weiss, M.P., Brown, T.L. (1980). Reconnaissance Geologic Map of the Mounds Quadrangle, Carbon and Emery Counties, Utah.

Gupta, H. V., Sorooshian, S., & Yapo, P. O. (1999). Status of automatic calibration for hydrologic models: Comparison with multilevel expert calibration. Journal of Hydrologic Engineering.

Hamilton E.L., Row P.B. (1949). Rainfall interception by chaparral in California.

Hettinger, R.D., & Kirschbaum, M.A. (2002). Stratigraphy of the Upper Cretaceous Mancos Shale (upper part) and Mesaverde Group in the southern part of the Uinta and Piceance basins, Utah and Colorado US Geological Survey.

Howes D.A., Abrahams A.D. (2003). Modeling runoff and runon in a desert shrubland ecosystem, Jornada Basin, New Mexico. Geomorphology 53:45-73.

Jackson, M.L., Barak, P. (2005). Soil chemical analysis: advanced course. UW-Madison Libraries Parallel Press.

Jackson W.L., Bentley R.G., Fisher S. (1984). Salinity Status Report, 1980-1982: Results of Bureau of Land Management Studies on Public Lands in the Upper Colorado River Basin, Technical Note Bureau of Land Management, Bureau of Land Management, Denver CO. pp. 62 p.

Jury, W.A., & Horton, R. (2004). Soil physics. John Wiley & Sons.

Kenney T.A., Gerner S.J., Buto S.G., Spangler L.E. (2009). Spatially referenced statistical assessment of dissolved-solids load sources and transport in streams of the Upper Colorado River Basin, USGS Scientific Investigations Report, U.S. Geological Survey, Reston, Virginia. pp. 50 p.

Laronne J.B., & Reid I. (1993). Very high-rates of bedload sediment transport by ephemeral desert rivers. Nature 366:148-150. DOI: 10.1038/366148a0.

Laronne, J.B., & Shen, H.W. (1982). The effect of erosion on solute pickup from Mancos Shale hillslopes, Colorado, USA. Journal of Hydrology, 59(1), 189-207.

Legates, D. R., & McCabe, G. J. (1999). Evaluating the use of “goodness-of-fit” measures in hydrologic and hydroclimatic model validation. Water Resources Research, 35(1), 233. doi:10.1029/1998WR900018.

Lin, A., Jackson, W.L, & Knoop, K.D. (1984). Storm runoff and water quality on three ephemeral washes in the Price River Basin, Utah. Journal of Soil and Water Conservation 39(3):211-214.

Loch, R.J. (2000). Effects of vegetation cover on runoff and erosion under simulated rain and overland flow on a rehabilitated site on the Meandu Mine, Tarong, Queensland. Soil Research, 38(2), 299-312.

Loope W.L. & Gifford G. (1972). Influence of a soil micro-floral crust on select properties of soils under pinyon-juniper in southeastern Utah. Journal of Soil and Water Conservation.

McGarigal, K. (2015). FRAGSTATS Help. University of Massachusetts, Amherst.

McGarigal, K., & Marks, B.J. (1995). Spatial pattern analysis program for quantifying landscape structure. Gen. Tech. Rep. PNW-GTR-351. US Department of Agriculture, Forest Service, Pacific Northwest Research Station.

McGwire, K.C., Taylor, K.C., Banta, J.R., & McConnell, J. R. (2011). Identifying annual peaks in dielectric profiles with a selection curve. Journal of Glaciology, 57(204), 763-769.

Mubarak A & Olsen RA (1977). A laboratory technique for appraising in situ salinity of soil. Soil Sci Soc Am J 41:1018–1020.

Myers, R.H., Montgomery, D.C., Vining, G.G., & Robinson, T.J. (2012). Generalized linear models: with applications in engineering and the sciences (Vol. 791). John Wiley & Sons.

Nash, J., & Sutcliffe, J.V. (1970). River flow forecasting through conceptual models part I—A discussion of principles. Journal of hydrology, 10(3), 282-290.

Navar J., Bryan R. (1990). Interception loss and rainfall redistribution by three semi-arid growing shrubs in northeastern Mexico. Journal of Hydrology 115:51-63.

Nearing, M. A., Wei, H., Stone, J. J., Pierson, F. B., Spaeth, K. E., Weltz, M. A., Flanagan, D.C., & Hernandez, M. (2011). A Rangeland Hydrology and Erosion Model. ASABE, 54(3), 901-908.

Nouwakpo, S. K., Weltz, M. A., and McGwire, K. (2015) Assessing the performance of structure-from-motion photogrammetry and terrestrial LiDAR for reconstructing soil surface microtopography of naturally vegetated plots. Earth Surf. Process. Landforms. DOI: 10.1002/esp.3787.

Paige, G.B., Stone, J.J., Smith, J.R., & Kennedy, J.R. (2004). The Walnut Gulch Rainfall Simulator: A Computer-Controlled Variable Intensity Rainfall Simulator. American Society of Agricultural Engineers, 20(1), 25-31.

Ponce II, S.L. (1975). Examination of a Non-point Source Loading Function For the Mancos Shale Wildlands of the Price River Basin, Utah. All Graduate Theses and Dissertations. Paper 3498.

Puigdefabregas J. (2005). The role of vegetation patterns in structuring runoff and sediment fluxes in drylands. Earth Surface Processes and Landforms 30:133-147. DOI: 10.1002/esp.1181.

Rao, B.K., Bowles, D.S., & Wagenet, R.J. (1984). Salt efflorescence in Price River basin. Journal of Environmental Engineering, 110(2), 457-471.

Rasely R.C., Roberts T.C., Pyper G.P. (1991). Upper Colorado River Basin Rangeland Salinity Control Project: Watershed Resource Condition Evaluation Phase II Procedure, Colorado River Basin Salinity Forum.

Reid I., Powell D.M., Laronne J.B. (1996). Prediction of bed-load transport by desert flash floods. Journal of Hydraulic Engineering 122:170-173. DOI: 10.1061/(ASCE)0733-9429(1996)122:3(170).

RHEM (2015). RHEM Parameter Estimation Equations. http://apps.tucson.ars.ag.gov/rhem/docs.

Riley J.P., Chadwick D.G., Dixon L.S., James L.D., Grenney W.J. (1982). Salt Uptake in Natural Channels Traversing Mancos Shales in the Price River Basin , Utah.

Robison, J., Bratrschovsky, K., Latcham, J., Morris, E., Palmer, V., & Villanueva, A. (2014). Challenge and response in the Colorado River Basin. Water Policy, 16.

Shen H.W. (1981). Role of sediment in non-point source salt loading within the upper Colorado River Basin: combined completion report, Colorado Water Resources Research Institute, Fort Collins, Colorado. pp. 213.

Shirinian-Orlando A.A., Uchrin C.G. (2000). A method for determining salt sources in surface waters. Journal of the American Water Resources Association 36:749-757. DOI: 10.1111/j.1752-1688.2000.tb04303.x.

Simanton, J.R., Weltz, M.A., & Larsen, H.D. (1991). Rangeland experiments to parameterize the water erosion prediction project model: vegetation canopy cover effects. Journal of Range Management, 276-282.

Slatyer R. (1965). Measurements of Precipitation Interception by an Arid Zone Plant Community (Acacia Aneura F. Muell) Unesco Arid Zone Research, Vol. 25, pp 181-192, 1956, 7 Fig, 2 Tab, 13 Ref, Disc.

Smith RE Goodrich DC, Woolhiser DA, Unkrich CL. (1995). Chapter 20: KINEROS: A kinematic runoff and erosion model. In Computer Models of Watershed Hydrology, 697 732. Singh VJ (ed.) Water Resources Publications: Highlands Ranch, CO.

Smith RE, Parlange JY. (1978). A parameter-efficient hydrologic infiltration model. Water Resources Research 14(3):533–538.

Thomas, Grant W. (1982). Exchangeable cations. In A.L. Page, R. H. Miller, and D. R. Keeney (eds.). Methods of soil analysis. Part 2. Chemical and microbiological properties. 2nd ed., Agron. Monogr. 9, ASA and SSSA, Madison, WI. p. 159-165.

Tuttle, M. L. W., Fahy, J. W., Elliott, J. G., Grauch, R. I., & Stillings, L. L. (2014). Contaminants from cretaceous black shale: I. natural weathering processes controlling contaminant cycling in mancos shale, southwestern united states, with emphasis on salinity and selenium. Applied Geochemistry, 46, 57-71. doi:10.1016/j.apgeochem.2013.12.010.

Tuttle, M. L. W., Fahy, J. W., Elliott, J. G., Grauch, R. I., & Stillings, L. L. (2014). Contaminants from cretaceous black shale: II. effect of geology, weathering, climate, and land use on salinity and selenium cycling, mancos shale landscapes, southwestern united states. Applied Geochemistry, 46, 72-84. doi:10.1016/j.apgeochem.2013.12.011.

United States Bureau of Reclamation (2005). Quality of Water Colorado River Basin, http://www.usbr.gov/uc/progact/salinity/pdfs/PR22.pdf2005, Progress Report No. 22.

United States Department of Agriculture – Natural Resources Conservation Service (2013). Web soil survey national cooperative soil survey, https://soilseries.sc.egov.usda.gov/OSD_Docs/P/PERSAYO.html.

United States Department of Agriculture – Natural Resources Conservation Service (2013). Web soil survey national cooperative soil survey, https://soilseries.sc.egov.usda.gov/OSD_Docs/C/CHIPETA.html.

Urgeghe A.M., Breshears D.D., Martens S.N., Beeson P.C. (2010). Redistribution of runoff among vegetation patch types: on ecohydrological optimality of herbaceous capture of run-on. Rangeland ecology & management 63:497-504.

Warner J.W., Heimes F.J., Middelburg R.F. (1985). Ground-water contribution to the salinity of the Upper Colorado River Basin, USGS Water-Resources Investigations Report, U.S. Geological Survey. pp. 113.

Wei H, Nearing MA, Stone JJ, Guertin DP, Spaeth KE, Pierson FB, Nichols MH, Moffett CA. (2009). A new splash and sheet erosion equation for rangelands. Soil Science Society of America Journal 73(4): 1386–1392.

Weltz, M., Nouwakpo, S.K., Rossi, C., Jolley, L., & Frasier, G. (2014). Salinity mobilization and transport from rangelands: assessment, recommendations, and knowledge gaps. General Technical Report 1. Reno, Nevada. 61.

Weltz, M. A., Jolley, L., Nearing, M., Stone, J., Goodrich, D., Spaeth, K.. . Wei, H. (2008). Assessing the benefits of grazing land conservation practices. Journal of Soil and Water Conservation, 63(6), 214.

West N.E. (1991). Nutrient cycling in soils of semiarid and arid regions. Semiarid lands and deserts: Soil resource and reclamation: 295-332.

Western Regional Climate Center. (2014). Cooperative Climatological Data Summaries. Retrieved from http://www.wrcc.dri.edu/climatedata/climsum/.

White R.B., Hawkins R.H. (1980). Non-point salt loading in a semi-arid watershed, Symposium on Watershed Management (21-23 July 1980). pp. 54-68.

Wilcox B., Davenport D., Pitlick J., Allen C. (1996). Runoff and erosion from a rapidly eroding pinyon-juniper hillslope, Los Alamos National Lab., NM (United States).

Wischmeier, W.H., & Smith, D.D. (1978). Predicting rainfall erosion losses-A guide to conservation planning. Predicting rainfall erosion losses-A guide to conservation planning.

Wood, M.K., & Blackburn, W.H. (1981). Grazing systems: their influence on infiltration rates in the Rolling Plains of Texas. Journal of Range Management, 331-335.

Wood, M.K., Jones, T.L., & Vera-Cruz, M.T. (1998). Rainfall interception by selected plants in the Chihuahuan Desert. Journal of Range management, 91-96.

Yapo P.O., Gupta H.V., Sorooshian S. (1998). Multi-objective global optimization for hydrologic models. Journal of Hydrology 204:83-97.

Zucca, C., Julitta, F., & Previtali, F. (2011). Land restoration by fodder shrubs in a semi-arid agro-pastoral area of Morocco. Effects on soils. Catena, 87(3), 306-312.

9 Appendix A

9.1 Price Vegetation Maps

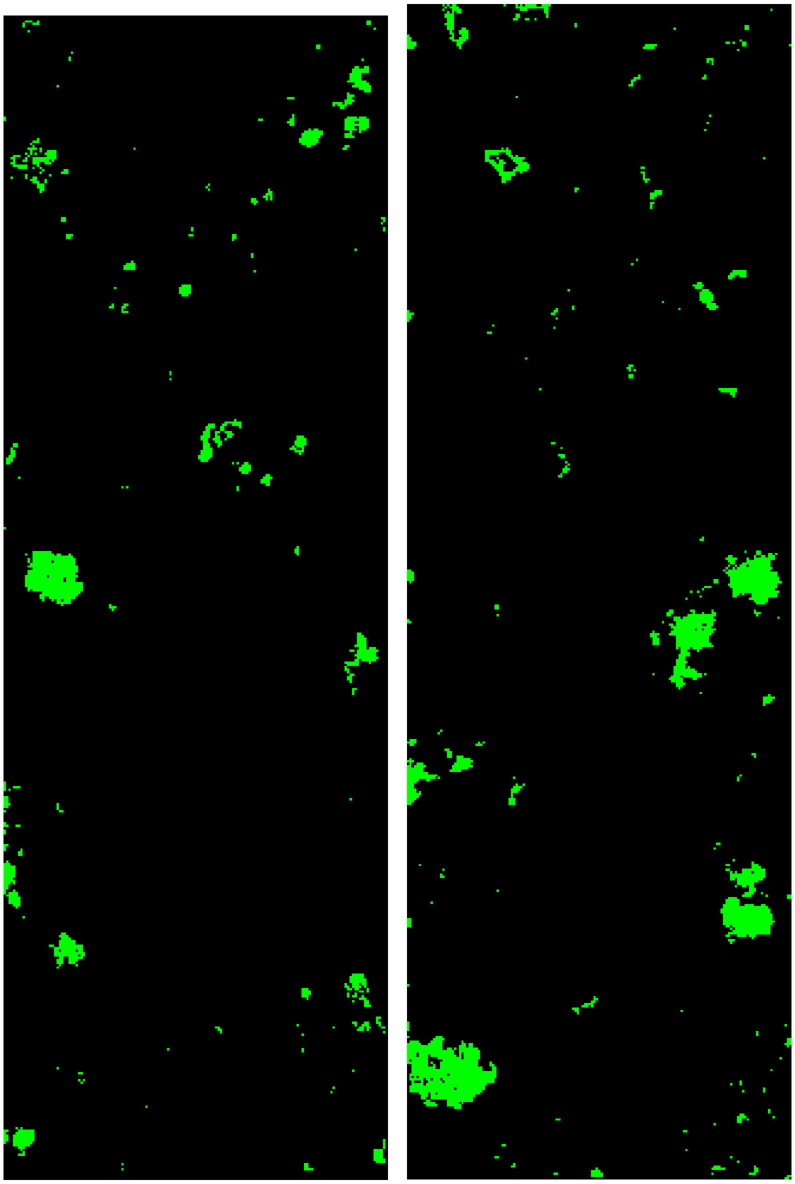

Figure 31a-b: Vegetation map of Price Plot 1 and 2 (left to right). Green = vegetation and black = soil.

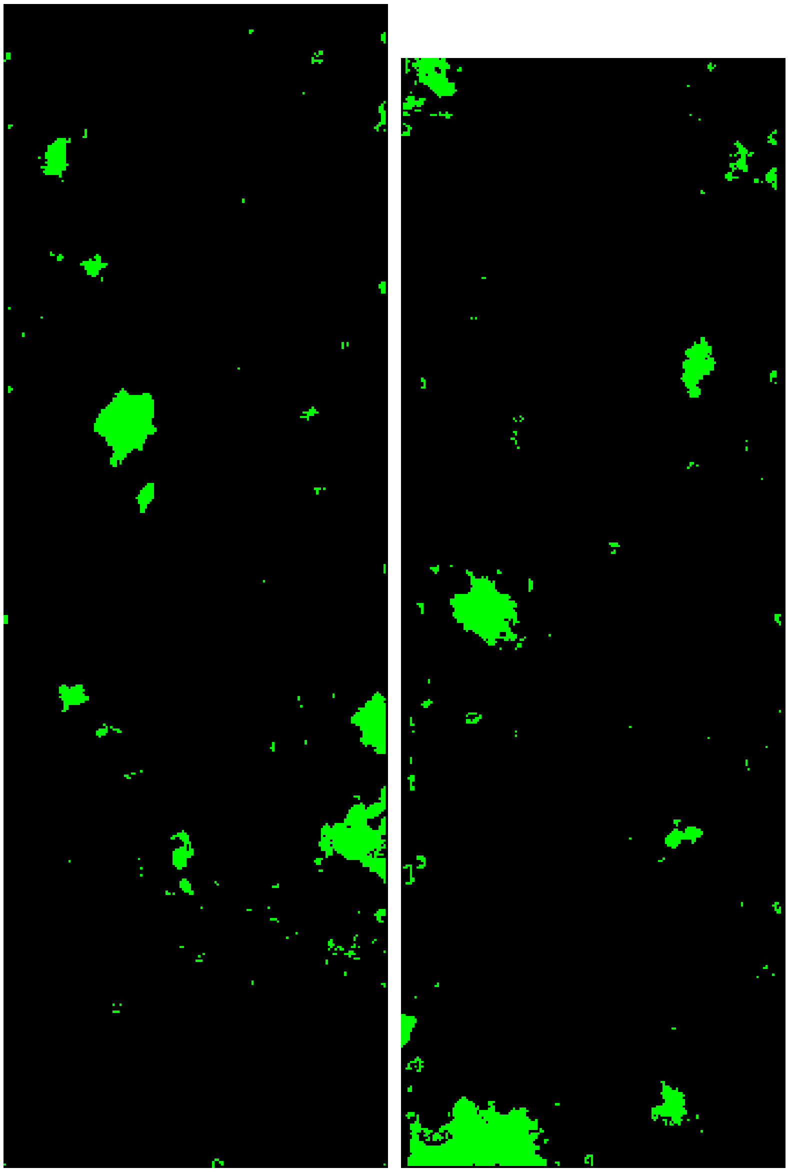

Figure 32a-b: Vegetation map of Price Plot 3 and 4 (left to right). Green = vegetation and black = soil.

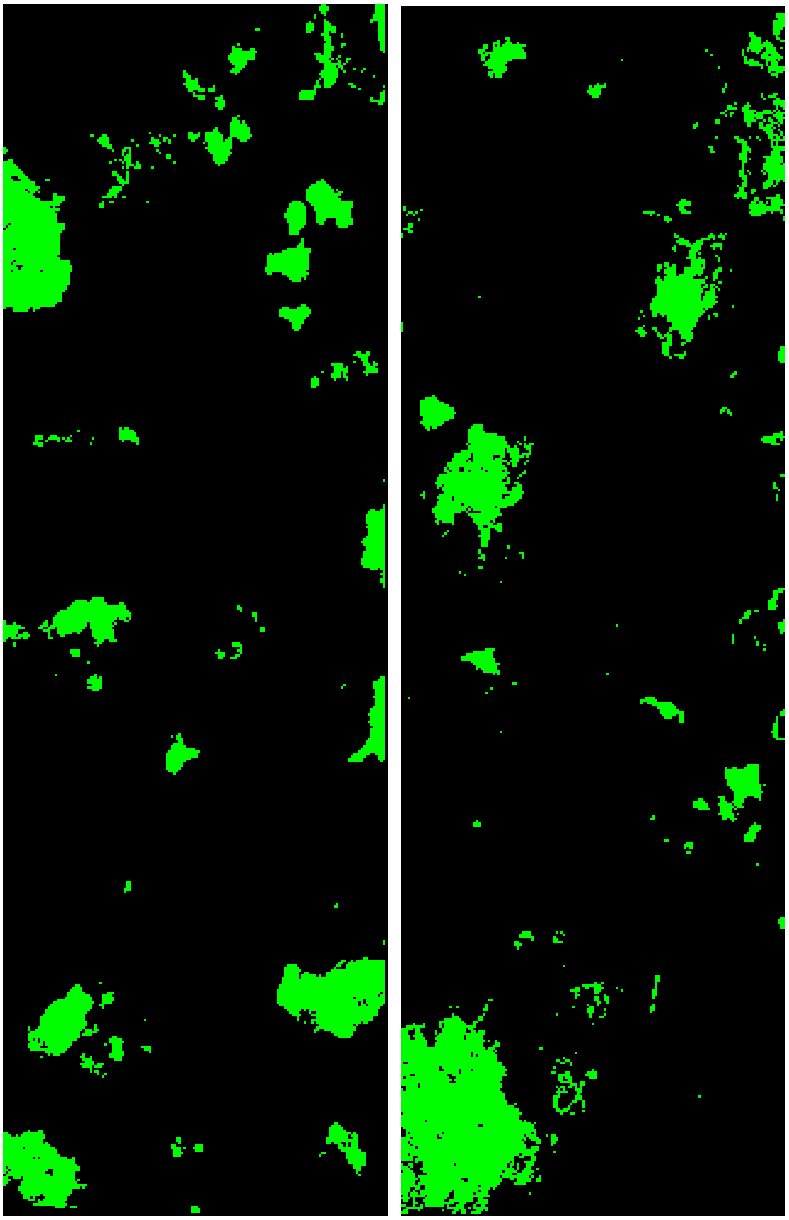

Figure 33a-b: Vegetation map of Price Plot 5 and 6 (left to right). Green = vegetation and black = soil.

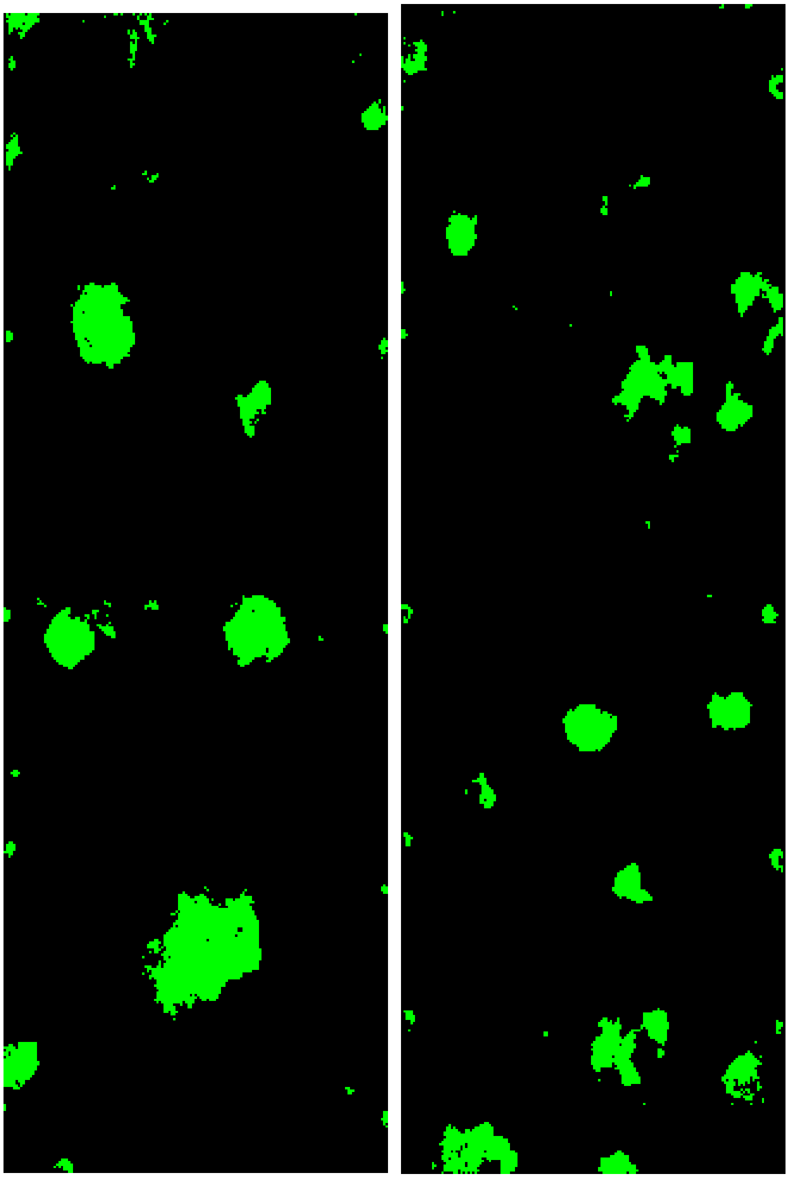

Figure 34a-b: Vegetation map of Price Plot 7 and 8 (left to right). Green = vegetation and black = soil.

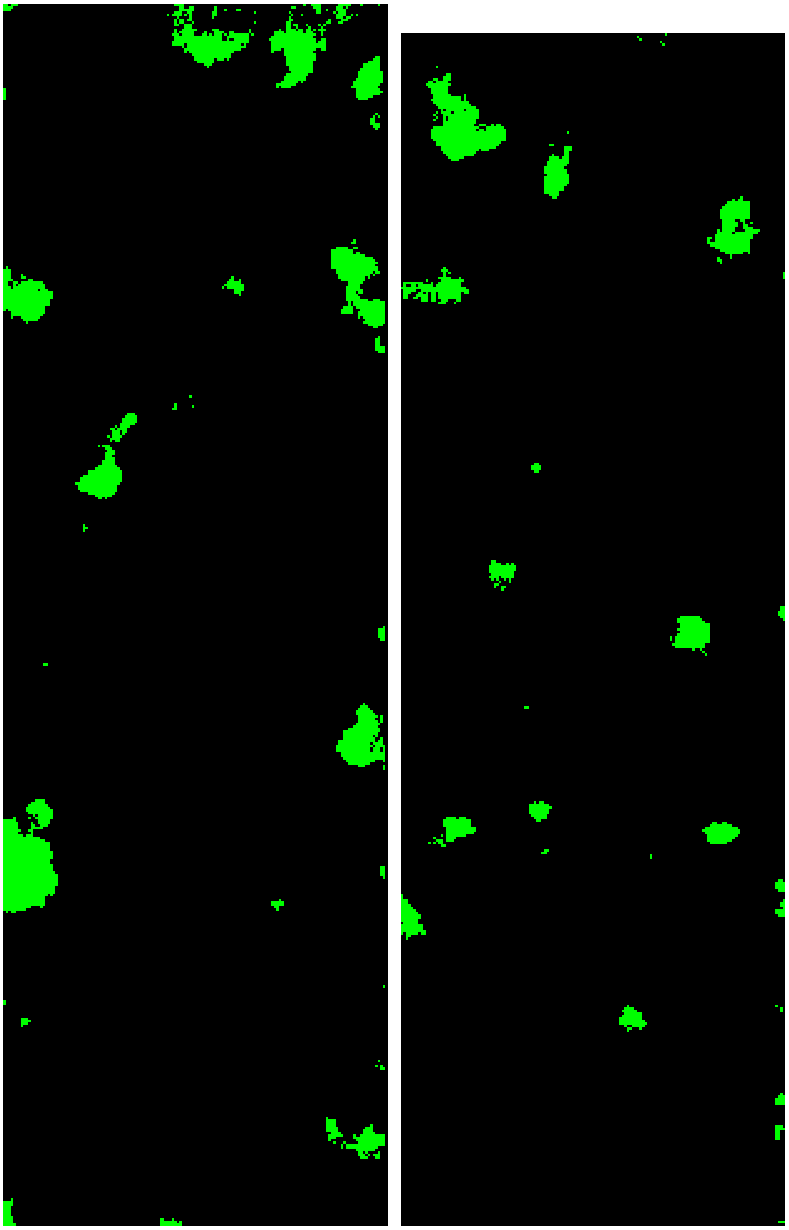

Figure 35a-b: Vegetation map of Price Plot 9 and 10 (left to right). Green = vegetation and black = soil.

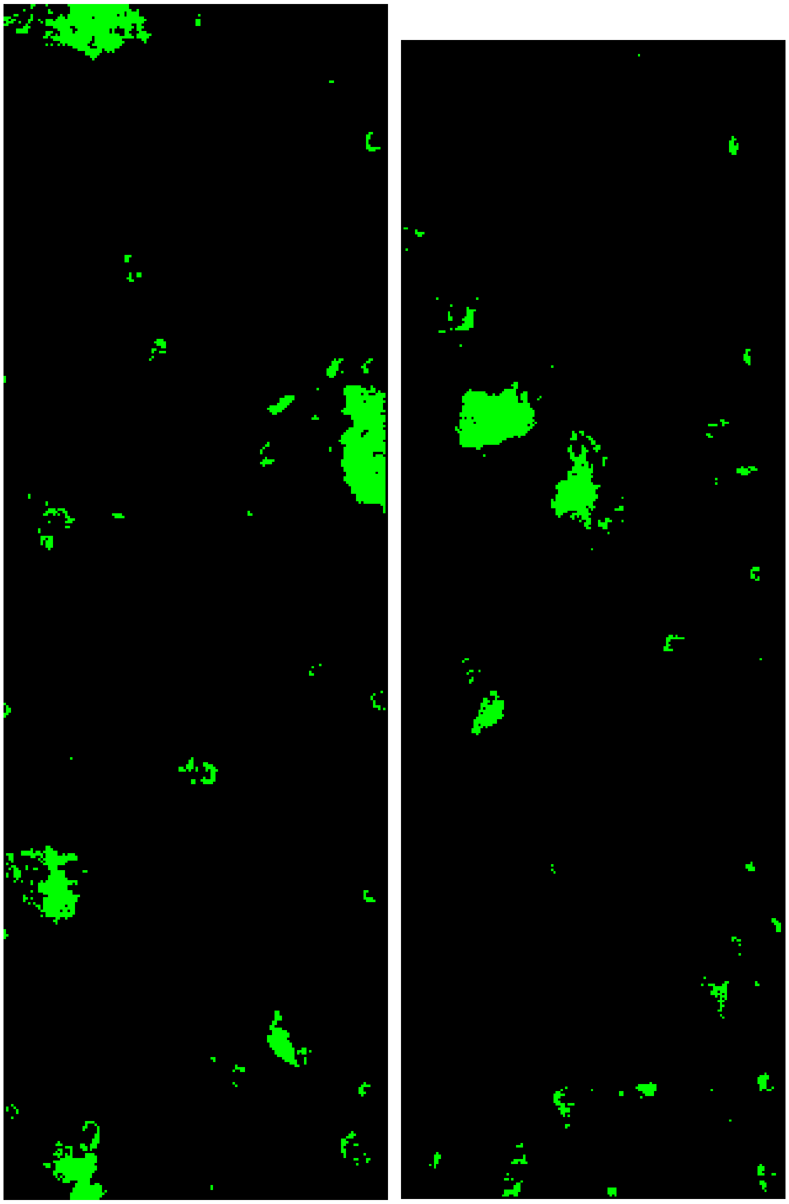

Figure 36a-b: Vegetation map of Price Plot 11 and 12 (left to right). Green = vegetation and black = soil.

9.2 Dry-X Vegetation Maps

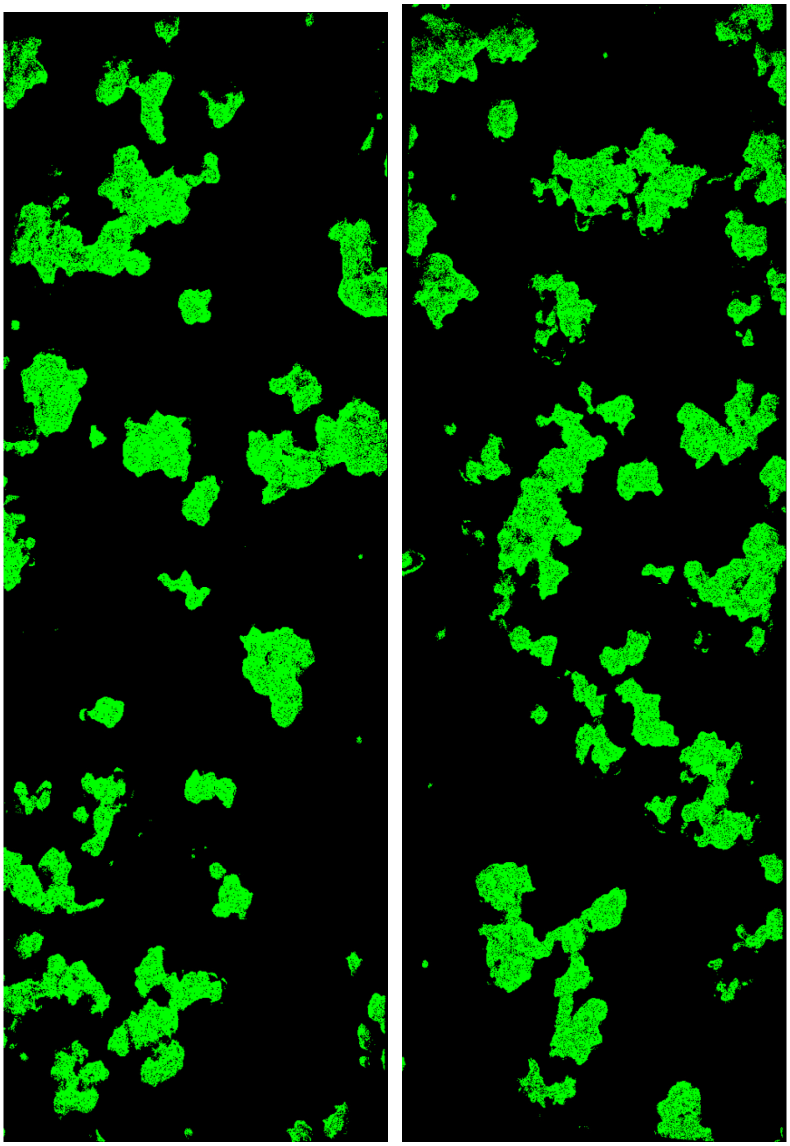

Figure 37a-b: Vegetation map of Dry-X Plot 1 and 2 (left to right). Green = vegetation and black = soil.

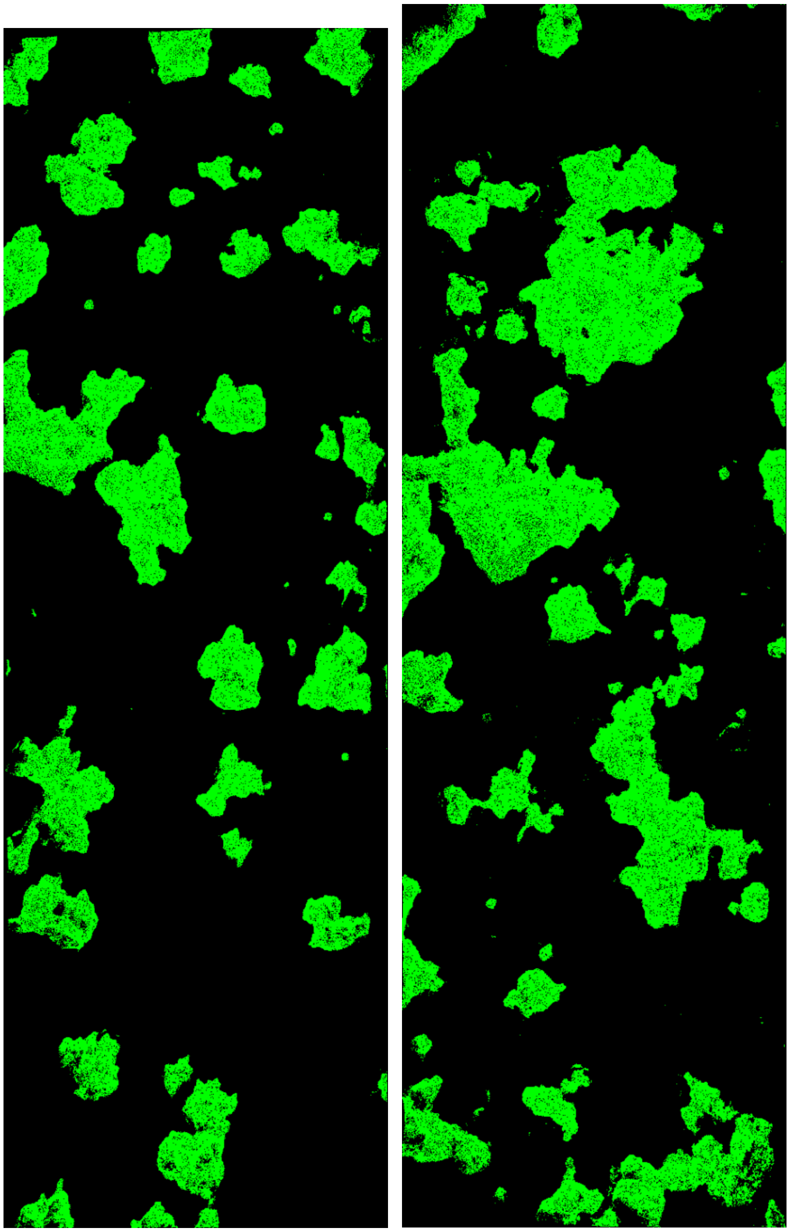

Figure 38a-b: Vegetation map of Dry-X Plot 3 and 4 (left to right). Green = vegetation and black = soil.

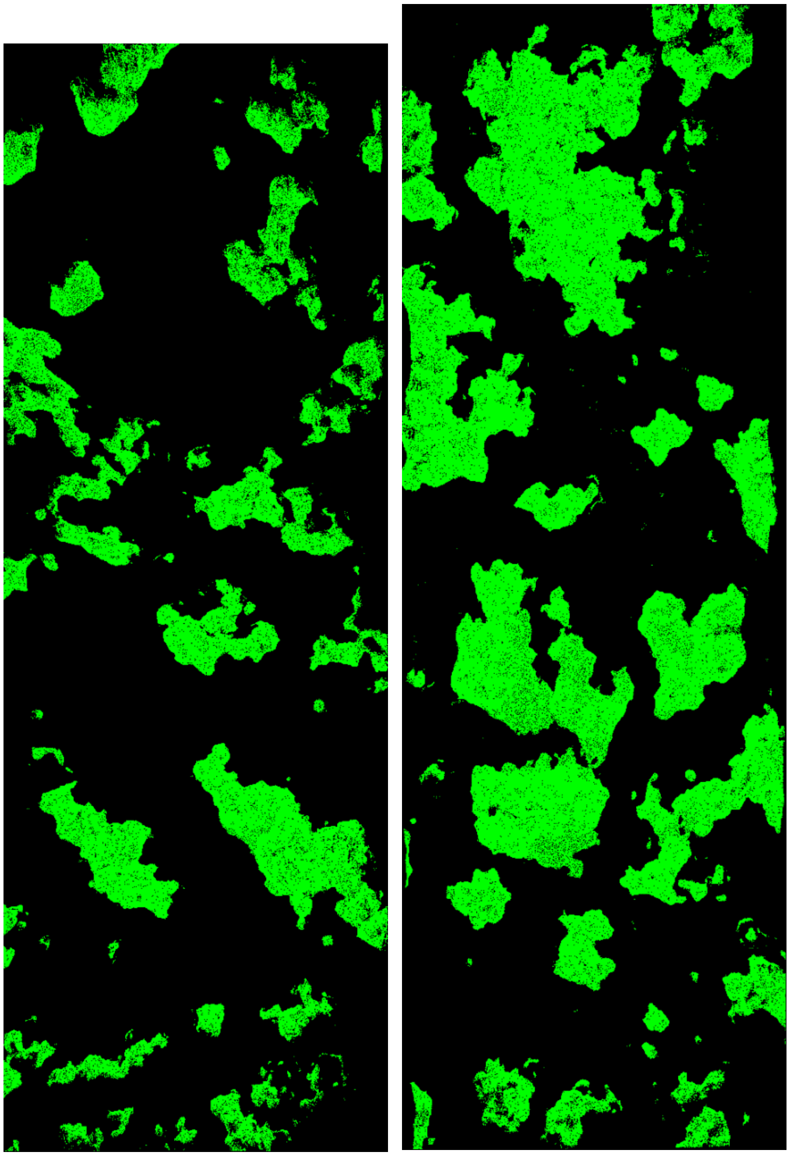

Figure 39a-b: Vegetation map of Dry-X Plot 5 and 6 (left to right). Green = vegetation and black = soil.

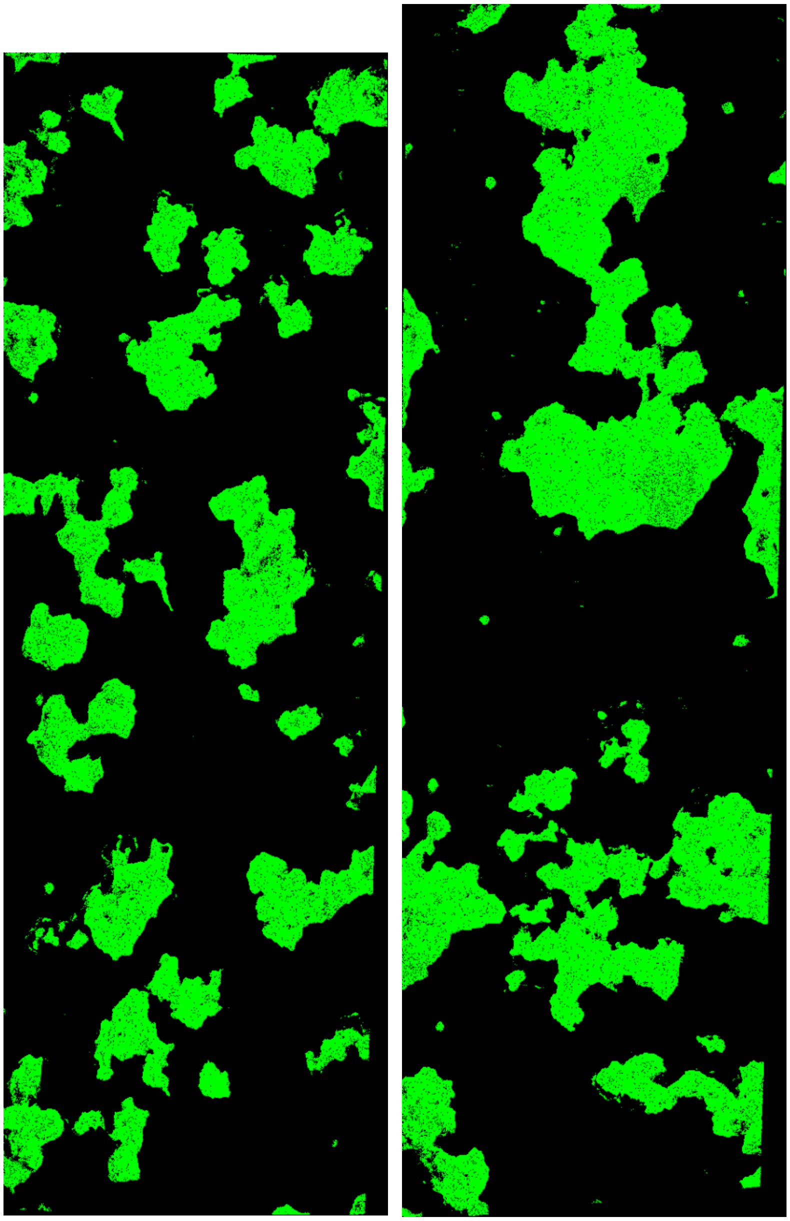

Figure 40a-b: Vegetation map of Dry-X Plot 7 and 8 (left to right). Green = vegetation and black = soil.

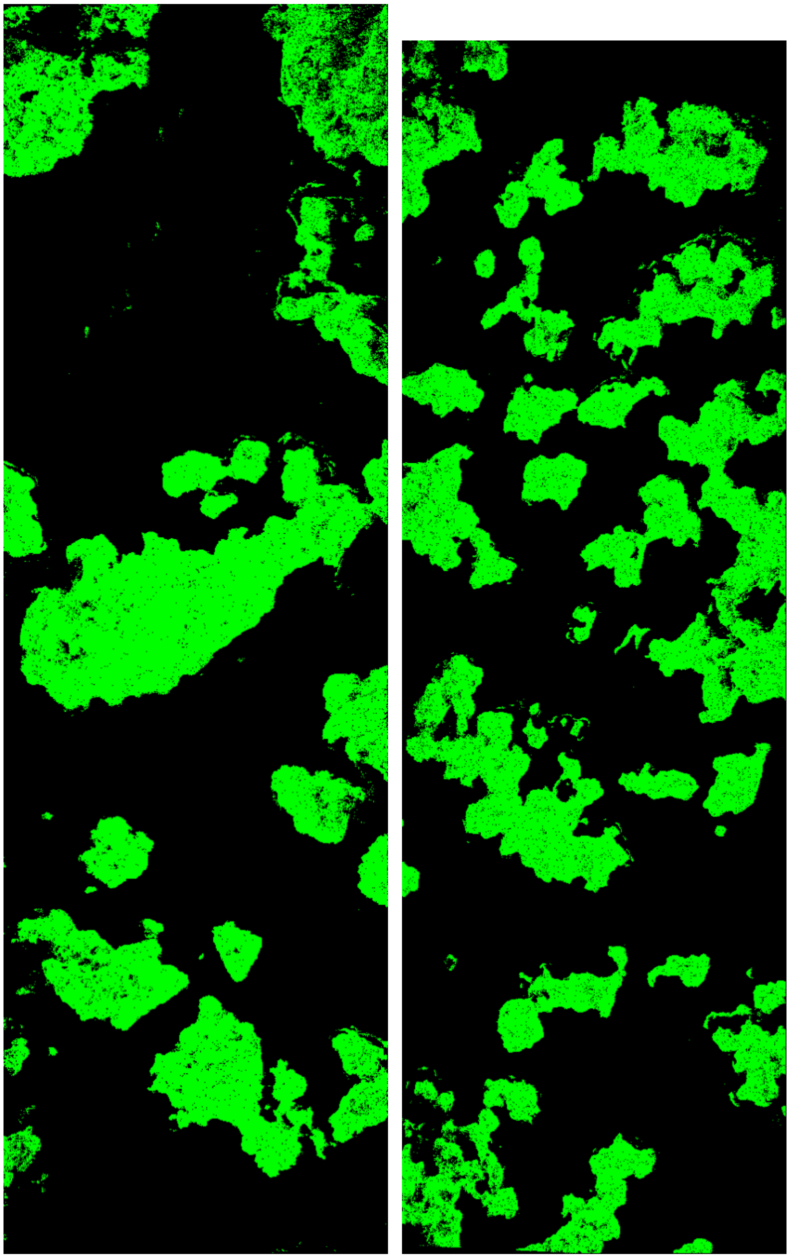

Figure 41a-b: Vegetation map of Dry-X Plot 9 and 10 (left to right). Green = vegetation and black = soil.

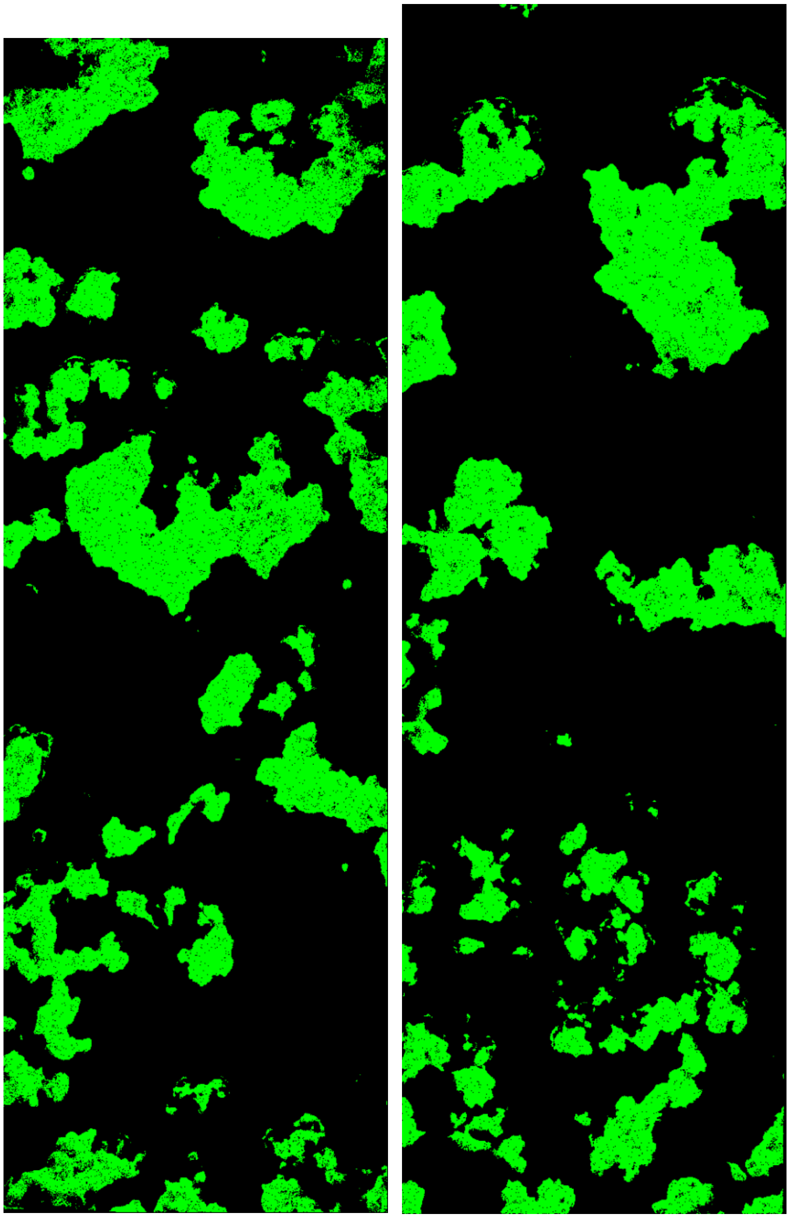

Figure 42a-b: Vegetation map of Dry-X Plot 11 and 12 (left to right). Green = vegetation and black = soil.

10 Appendix B

10.1 RHEM Input File Parameter Descriptions (! separates parameter value from text)

! Uniform Hillslope
BEGIN GLOBAL
CLEN = ! The characteristic length of the hillslope in meters or feet
UNITS = ! Metric or English units
DIAMS = ! List of representative soil particle diameters (mm or in) for up to 5 particle classes
DENSITY = ! List of densities (g/cc) corresponding to the above particle classes
TEMP = ! Temperature in degrees C. Not used by RHEM
NELE = ! Number of hillslope elements (planes)
END GLOBAL

BEGIN PLANE
ID = ! Identifier for the current plane
LEN = ! The plane slope length in meters or feet
WIDTH = ! The plane bottom width in meters or feet
CHEZY = ! overland flow Chezy Coeff. (m^(1/2)/s) (square root meter per second)
RCHEZY = ! concentrated flow Chezy Coeff. (m^(1/2)/s) (square root meter per second)
SL = ! slope expressed as fractional rise/run
SX = ! normalized distance
CV = ! Coefficient of variation for KE
SAT = ! Initial degree of soil saturation, expressed as a fraction of the pore space filled
PR = ! print flag
KSS = ! splash and sheet erodibility coeff.
KOMEGA = ! undisturbed concentrated erodibility coeff. (s2/m2)
KCM = ! maximum concentrated erodibility coeff. (s2/m2)
CA = ! Cover fraction of surface covered by intercepting cover - rainfall intensity is reduced by this fraction until the specified interception depth has accumulated
IN = ! Interception depth in mm or inches
KE = ! Effective hydraulic conductivity (mm/h)
G = ! Mean capillary drive, mm or inches — a zero value sets the infiltration at a constant value of KE
DIST = ! Pore size distribution index. This parameter is used for redistribution of soil moisture during unponded intervals
POR = ! Porosity
ROCK = ! Volumetric rock fraction, if any. If KE is estimated based on textural class it should be multiplied by (1 - Rock) to reflect this rock volume
SMAX = ! Upper limit to SAT
ADF = ! Beta decay factor in the detachement equation in Al-Hamdan et al 2012 (Non-FIRE)
ALF = ! allow variable alfa in the infiltration Smith-Parlange Equation, alf <= 0.05, Green and Ampt
BARE = ! fraction of bare soil to total area
RSP = ! Rill spacing in meters or feet
SPACE = ! average micro topographic spacing in meters or feet
RELIEF = ! Average micro topographic relief in mm or inches
FRACT = ! List of particle class fractions - must sum to one
END PLANE

Link: http://apps.tucson.ars.ag.gov/rhem/docs

11 Appendix C

11.1 Landscape Metrics Histograms

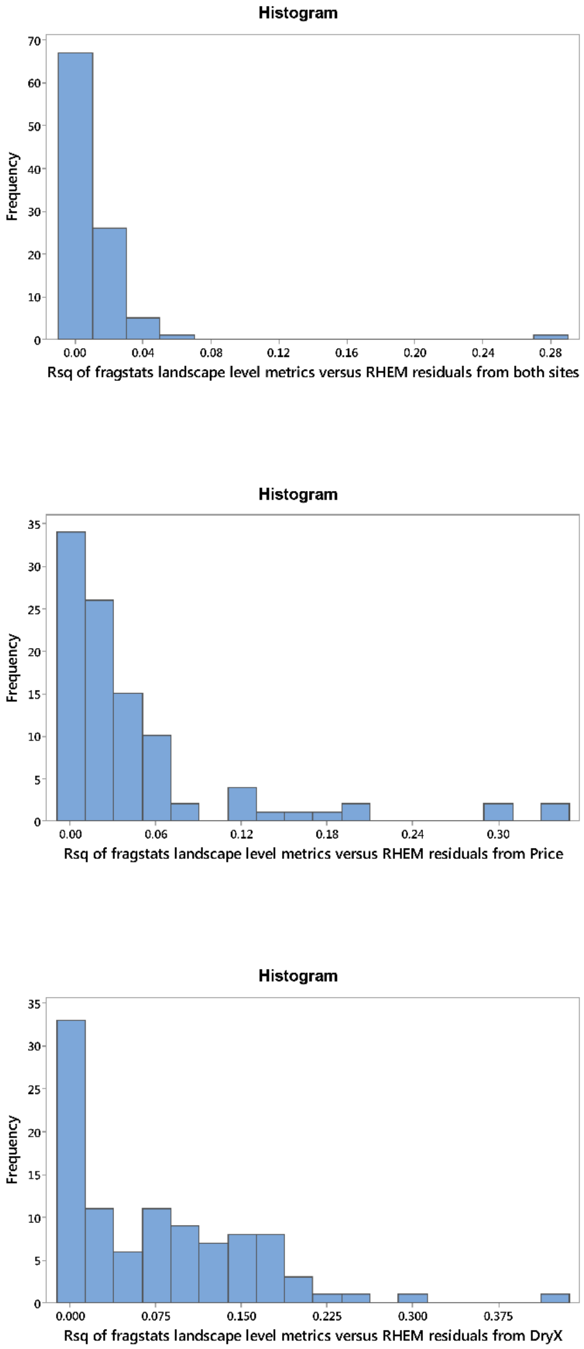

Figure 43a-c: Histograms of landscape level metrics for both sites, Price, and Dry-X.

11.2 Soil Class Metrics Histograms

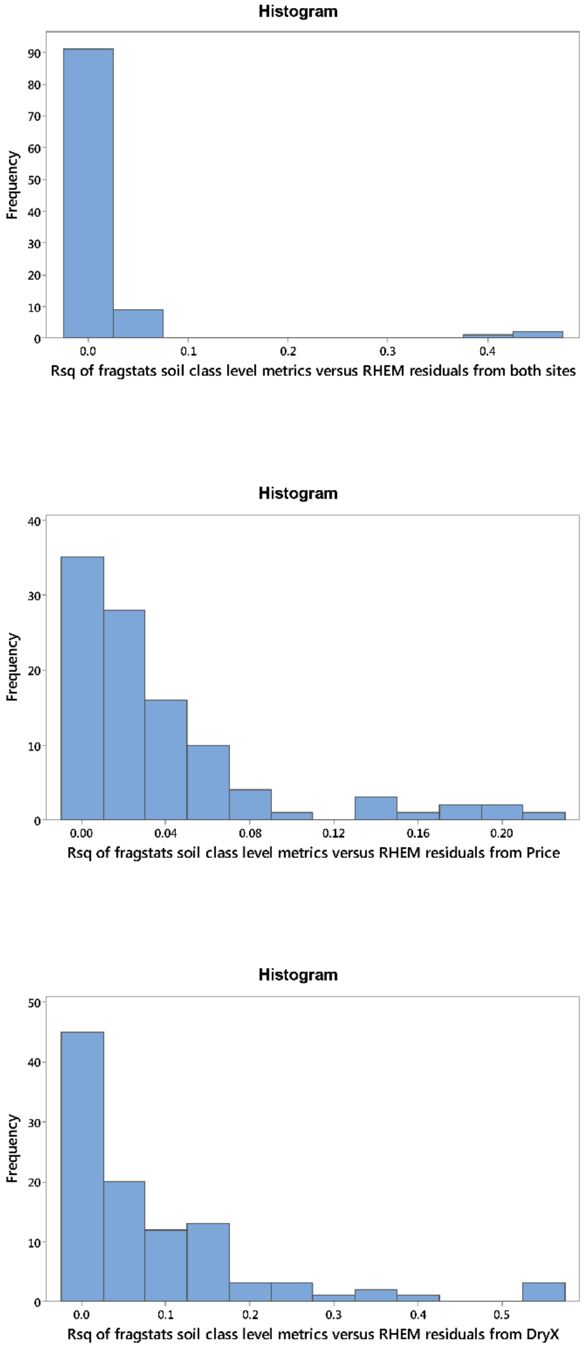

Figure 44a-c: Histograms of soil class level metrics for both sites, Price, and Dry-X.

11.3 Vegetation Class Metrics Histograms

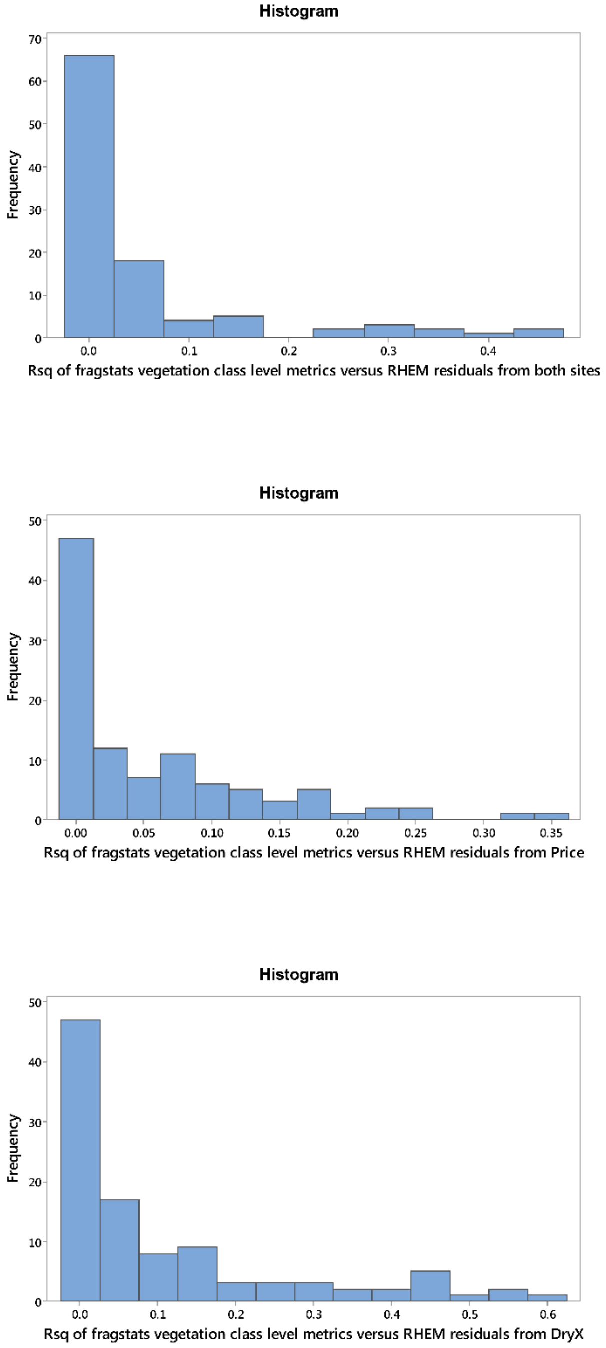

Figure 45a-c: Histograms of vegetation class level metrics for both sites, Price, and Dry-X.